OPEN ACCESS
OPUS AUGSBURG

Universität Augsburg
Universitätsbibliothek

# Physics and applications of self-assembled quantum dots

**E. Beham, Markus Betz, Stephan Trumm, M. Kroutvar, Y. Ducommun, Hubert J. Krenner, Max Bichler, A. Leitenstorfer, Jonathan J. Finley, Artur Zrenner, Gerhard Abstreiter**

**Angaben zur Veröffentlichung / Publication details:**

Beham, E., Markus Betz, Stephan Trumm, M. Kroutvar, Y. Ducommun, Hubert J. Krenner, Max Bichler, et al. 2004. "Physics and applications of self-assembled quantum dots." *physica status solidi (c)* 1 (8): 2131–59. https://doi.org/10.1002/pssc.200404764.

**Nutzungsbedingungen / Terms of use:**

**licgercopyright**

*Dieses Dokument wird unter folgenden Bedingungen zur Verfügung gestellt: / This document is made available under these conditions:*
***Deutsches Urheberrecht***
*Weitere Informationen finden Sie unter: / For more information see:*
*https://www.uni-augsburg.de/de/organisation/bibliothek/publizieren-zitieren-archivieren/publiz/*

# Physics and applications of self-assembled quantum dots

**E. Beham**[1], **M. Betz**[*,2], **S. Trumm**[2], **M. Kroutvar**[1], **Y. Ducommun**[1], **H. J. Krenner**[1], **M. Bichler**[1], **A. Leitenstorfer**[**,2], **J. J. Finley**[1], **A. Zrenner**[3], and **G. Abstreiter**[1]

[1] Walter-Schottky-Institut, Technische Universität München, 85748 Garching, Germany
[2] Physik-Department E11, TU München, James-Franck-Str., 85748 Garching, Germany
[3] Department Physik, Universität Paderborn, Warburger Strasse 100, 33098 Paderborn, Germany

Linear and nonlinear spectroscopic invsetigations of self-assembled quantum dots open up the possibility to study model quantum mechanical systems with potential applications in solid-state based quantum information processing. In this article we review recent advances in our understanding of the physics of self-assembled quantum dots and novel devices based upon them. We focus our attention on four key areas: (i) Investigations of individual quantum dots using photocurrent absorption spectoscopy (ii) The study of coupled pairs of electronically coupled quantum dots with field tunable coupling. (iii) Femtosecond experiments on small ensembles of quantum dots which demonstrate potential for quantum-coherent operations and (iv) applications of quantum dots in novel devices for wavelength selective optical data storage.

## 1 Introduction and historical overview

The revolution in information technology over the past few decades has undeniably had a more profound impact on human society than any other area of science. Most of key components are based on semiconductor devices with electronic or opto-electronic functionality. After decades of research and development, such semiconductor devices are now approaching the fundamental limits of miniaturization; charge carriers can be fully localized within quasi-zero dimensional heterostructures, termed quantum dots (QDs), and quantum mechanics entirely dictates functionality. From a technological perspective, the most direct and flexible way to produce QDs is to lithographically pattern an existing two-dimensional (2D) semiconductor heterostructure. This can be achieved either physically by etching or electrostatically using specially designed metallic gate structures. The latter approach has been enormously successful for electronic applications such as single electron devices [1] but cannot provide simultaneous confinement for electrons and holes. By comparison, studies of optically active QDs were pioneered within SFB-348 during the early 1990s using locally inter-diffused structures [2], natural quantum dots formed by local potential fluctuations in narrow quantum wells [3, 4, 6] or etched QW structures [7]. Whilst these early works provided first key experimental demonstrations of nanostructures with zero-dimensional character, the necessary patterning steps were often found to introduce defects at the crystal surface which degrade optical performance.

In the intervening decade, strain driven self-assembly has emerged as the principle fabrication technique for QDs with high optical quality [8]. Such QDs are formed via the Stranski–Krastanov (S–K)

* Corresponding author: e-mail: mbetz@ph.tum.de, Fax: +49 89/289-12842, Tel.: +49 89/289-12861
** Now at Universität Konstantz, Germany.

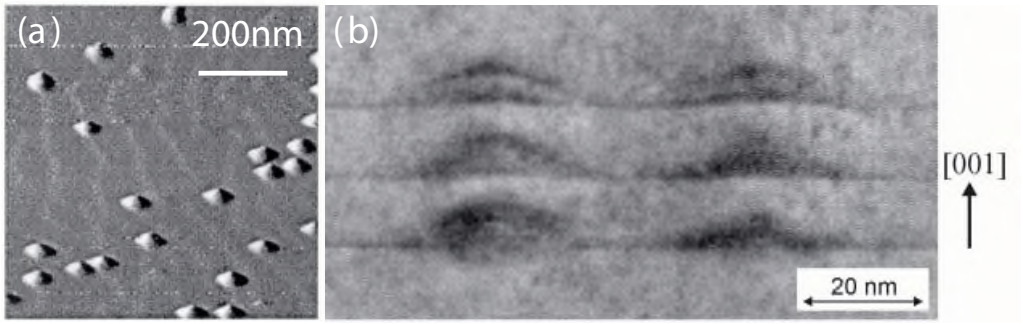


**Fig. 1** a) AFM image of a sparse array of In(Ga)As S–K QDs deposited on GaAs. b) High resolution TEM cross-section of vertically correlated InAs–GaAs QDs via multilayer Stranski–Krastanov growth.

growth mode that occurs during lattice mismatched heteroepitaxy [9]. In this review, we will focus exclusively on the most commonly investigated GaAs–In(Ga)As heterosystem for which the lattice mismatch is $\leq 7.2\%$. In(Ga)As can be deposited on GaAs in atomically smooth, compressively strained layers up to the critical thickness of a few atomic monolayers (ML). Island nucleation takes place at a coverage of about $\sim$1.8ML for InAs–GaAs or $\sim$8ML for $In_{0.5}Ga_{0.5}As$–GaAs, respectively [10, 11]. The morphological phase transition from layer by layer growth to 3D-islands on a wetting layer occurs spontaneously and is driven by the minimization of total free energy caused by the larger reduction of the elastic energy compared with the increase of the surface energy of the islands [11]. The resulting islands are coherent (defect free), have high areal densities up to about $\sim 10^{11}$ cm$^{-2}$ and, more importantly, have typical sizes in the $\sim$ 10 nm range giving rise to large confinement energies for both electrons and holes [16–19]. Figure 1a shows a typical surface topology of such QDs measured using AFM on dots formed by depositing 5 ML InAs on GaAs at $T_g \sim 500$ °C and a low InAs growth rate of 0.02 ML/s. The dots have a typical lateral size of $\sim$10–20 nm and height of $\sim$5–8 nm. In addition to the most commonly investigated In(Ga)As–GaAs materials system, Stranski–Krastanow growth has now also been demonstrated in other strained III–V (InP/InAs [12], GaAs/InGaAlSb [13] and GaSb/InSb [14]), group IV (Si/Ge [5]) and II–VI [15] materials systems illustrating the widespread applicability of the technique.

At low temperatures the inter-band optical response of large ensembles of self-assembled quantum dots are complicated by large inhomogeneous broadening effects (typically $\geq$15 meV) arising from naturally occurring dot-dot size, shape and morphology fluctuations. In contrast, individual self-assembled QDs possess a discrete, homogeneously broadened optical spectrum reflecting their fully quantized electronic structure. Over the past decade, sophisticated optical techniques developed within *SFB-348* have been shown to be capable of probing individual QDs [3, 20, 45]. Such techniques have enabled investigation of a rich spectrum of zero-dimensional physical phenomena and few-carrier properties in the absence of inhomogeneous broadening phenomena. Specific examples include the direct study of few-particle interactions in neutral [22, 28, 44, 47, 48, 74] and charged QDs [39–43], enhanced coupling to phonons [23, 29] and nuclear spins [21] and more recently Rabi oscillations of the interband optical polarization [31, 54, 55]. The latter development is potentially the most interesting of all since Rabi oscillations represent a fundamental one quantum bit (qubit) operation [31, 34] on the basis of a charge exciton in a QD. This demonstration of the basic ingredient for quantum logic paves the way for future QD-based implementations of quantum information processing based on charge and spin [24] degrees of freedom and perhaps conditional quantum logic in coupled QD systems [35–37].

In multilayer S–K structures, strain fields reaching the growth surface during heteroepitaxy also influence the nucleation of islands in subsequently deposited layers. Relaxation of compressive island strain results in a slight increase of the lateral lattice constant in the matrix material immediately above the buried islands. As a result, In(Ga)As deposited during a subsequent growth phase can then

accumulate preferentially in this region due to the reduced strain energy. This local material accumulation causes a reduction of the nominal critical coverage for island nucleation and vertically correlated chains of islands can be controllably fabricated [18, 26]. Figure 1(b) shows a typical cross-sectional transmission electron microscopy (TEM) image of such stacked InAs–GaAs quantum dots fabricated using this modified S–K growth mode. The stacked InAs islands are found to be vertically correlated with a high probability and a separation of only a few ∼nm giving rise to coupled electronic states. Furthermore, the island sizes in subsequently deposited QD layers are found to be remarkably homogeneous due to the strain modified chemical potential on the growth surface. In general, the average island size is observed to increase as subsequent QD-layers are deposited since the effective critical thickness is modified by the pre-strained substrate. This effect can, however, be strongly reduced by controllably adjusting the growth conditions as successive QD-layers are deposited as demonstrated in Ref. [27] and the present work. The formation of vertically correlated S–K islands in multiple layer structures provides a very efficient route towards electronic coupled zero dimensional systems. Electronic coupling and significant Coulomb interaction of electronic states in neighboring dots are expected to become important for separations below ∼10 nm. Recent, single QD-molecule spectroscopy has already revealed evidence for such interdot electronic coupling [28].

In the present article, we review the progress in our understanding of the fundamental physics of QDs and QD-molecules formed by Stranski–Krastanow growth and discuss a number of novel applications and devices. We begin in Section 2 by presenting results of single dot absorption spectroscopy with potential applications to readout the result of quantum-coherent manipulations on single self-assembled InAs/AlGaAs QDs [56]. Section 3 focuses on the controlled coupling of the zero-dimensional states in pairs of stacked QDs tunable via an applied external electric field. Our measurements indicate a strong dependency of the coupling strength on the relative energetic position of the electronic states in the constituents of the artificial molecule and on the intrinsic coupling strength, defined by the spacer thickness between the two-QD layers. This is followed in Section 3 by sensitive femtosecond experiments on both large ensembles and individual QDs, providing an interesting insight into the ultrafast relaxation processes of electronic excitations within the QDs. First experimental results of a two-color femtosecond experiment on a system consisting of only a few QDs are presented, demonstrating the realizability of quantum-coherent operations via this experimental scheme. Finally, in Section 4 we describe the application of InGaAs QDs as novel optically switchable memory structures. We demonstrate that single charges (electrons or holes) can be controllably optically generated within individual QDs via frequency selective optical excitation. Stored charges are found to have extremely long lifetimes at low temperature (hours at $T = 100$ K). Such devices may provide a direct route to transfer between spin and optical polarization for future applications in quantum information processing.

## 2 Single dot photodetectors

Most QD-based devices such as injection lasers, detectors and memory structures utilize large ensembles of self-organized QDs. Until now, inhomogeneous broadening effects arising from dot-dot size and composition fluctuations could not be reduced below ∼15 meV using standard S–K growth [19] and the potential offered by zero-dimensionality cannot be fully realized. A similar argument applies for inter-band photodetectors and it may be easier to engineer useful devices which are based on a single QD – so called single quantum dot photodiodes. With a single QD photodiode it is possible to benefit from the sharp spectral absorption features of semiconductor artificial atoms as known from the field of single QD spectroscopy [20]. The basic concept underpinning the operation of this device is sketched in Fig. 2.

The principal allowed inter-band transitions in a QD occur between shells with equal principal quantum number $n$ – Fig. 2a. The resulting absorption lines are sharp spectral features with homogeneously broadened (lifetime limited) linewidth Fig. 2b. At high internal electric fields (typically = 40 kV/cm in the GaAs/InGaAs material system), the carrier tunneling time $\tau_t$ out of the QD is shorter

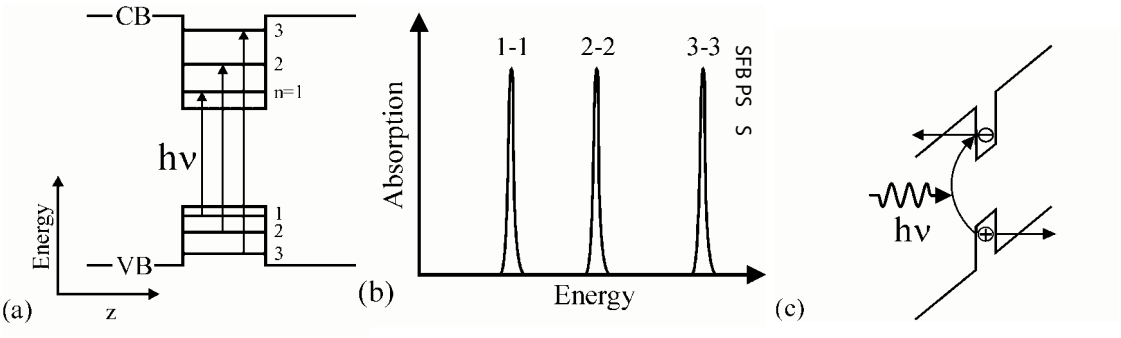


**Fig. 2** a) Schematic single particle level scheme of a semiconductor QD. Optical interband absorption results mainly from transitions among levels with equal main quantum number *n*. b) The absorption spectrum is delta-function like, the individual lines are clearly separated. c) Under the influence of high electric fields photoexcited electron–hole pairs will be separated by tunneling prior to spontaneous recombination and hence contribute to photocurrent.

as the radiative lifetime $\tau_r$ as shown in Fig. 2b. According to $\tau_T^{-1} = \tau_r^{-1} + \tau_t^{-1}$, the total decay rate $\tau_T^{-1}$ will be dominated by tunneling under this condition. At sufficiently small tunneling times, effectively each exciton generated by an elementary absorption process will be photoionized by tunneling. In the external circuit this process is detected as separation of a single electron–hole pair and hence as a photocurrent (PC), which is equivalent to the flow of a single elementary charge $e$ through the structure. The maximum photocurrent that can be obtained from a resonantly excited single QD photodiode will depend on the rate at which successive cycles of absorption and photoionization can be performed. As will be presented in the following sections, the tunneling time $\tau_t$ can be tuned by the external bias voltage $V_B$ from infinity down to the $\sim$ ps range. From this, it is clear that the amount of photocurrent from a single QD photodiode can easily exceed $\sim$ 10 nA. We continue by describing specific features of single QD photodiodes. Following this, we will generalize the underlying concept and describe the single QD photodiode as a single 2-level system with electric contacts. Thereby we will show, that such systems can provide a completely new optoelectronic functionality in the coherent regime.

### 2.1 Absorption spectroscopy of individual quantum dots

From a technological point of view, a single QD photodiode consists of a QD embedded typically in the intrinsic region of a p–i–n or n(p)–i-Schottky diode with optical access. Such an arrangement allows for different types of applications, such as PL-experiments as a function of electric field [40], optically detected single dot charging [39, 41–43], single QD light emitting devices [44, 46] or single dot PC spectroscopy first demonstrated by Beham et al using local Schottky contacts induced by metallic scanning probes [47, 48]. We now describe new single dot device concepts, based on structures defined by lithographic techniques. For controlled tuning of the electric field, the QDs are embedded in the intrinsic region of a n–i-Schottky diode (see Fig. 3). The band diagram under reverse bias condition (negative $V_B$ on the Schottky contact with respect to the back contact) is shown schematically in Fig. 3a. The sample was grown by molecular beam epitaxy on a $n^+$-GaAs substrate. Nominally 8 monolayers of $In_{0.5}Ga_{0.5}As$ have been deposited at 530 °C on an intrinsic layer (here GaAs) above the n-doped GaAs layer ($5 \times 10^{18}$ cm$^{-3}$). The width and exact composition of the i-layers was varied to match the specific requirements for different experiments. From AFM measurements on uncapped reference samples we determined dot densities in the range of $1 \times 10^{10}$ cm$^{-2}$ and an average dot height of 4 nm.

The samples are processed as photodiodes combined with near field shadow masks as shown schematically in Fig. 3b. Electron beam lithography and a dry chemical etch process ($SiCl_4$) are employed

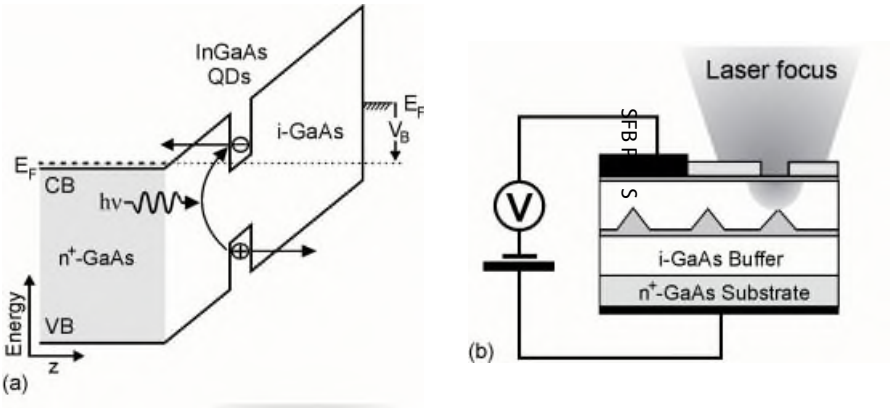


**Fig. 3** a) Schematic band diagram of a n–i-Schottky diode. For detection of QD PC a reverse bias voltage is applied. b) Device structure of a single QD photodiode. The QDs are embedded in a n–i-Schottky diode with a near field shadow mask providing spatialy selective optical access.

to define an aluminum shadow masks with apertures ranging from 150 to 500 nm in diameter. As a top contact we use a 5 nm thick semitransparent Ti layer (optical transmission ∼50%) below the electrically isolated shadow mask to achieve homogeneous electric field in the region of the investigated QD. For the back contact a Ge/Au/Ni/Au film was deposited and alloyed. For this device the whole mesa structure ($300 \times 400$ μm) is contacted electrically, but only the QD under the selected aperture is probed optically in PC and PL experiments. The devices were mounted in a confocal low-temperature microscope for analysis (see Ref. [45] for details) operated at temperatures down to $T = 2.3$ K. In the PC experiments we used a power stabilized cw Ti:Sapphire laser for resonant optical excitation of the QDs and a current–voltage converter for detection of the photocurrent. For additional non-resonant PL measurements, we used a HeNe laser (632.8 nm), a 0.7 m Dilor spectrometer, and a cooled CCD camera for detection.

Experimentally either PC or PL can be studied, depending on the external bias voltage $V_B$ applied to the sample as sketched in Fig. 3b. For $V_B \leq -1$ V, which corresponds to an internal electric field $F \geq 50$ kV/cm, the tunneling time $\tau_t$ of the photo excited carriers out of the QD is already much shorter than the radiative lifetime $\tau_r$. In this regime most of the carriers contribute to the PC. With increasing $V_B$ the electric field is reduced, which results in an increase of $\tau_t$. Since $\tau_r$ is in first order independent on electric field we expect a transition from the regime of PC to the regime of PL. In Fig. 4 we present PL and PC spectra as a function of $V_b$ taken at the same aperture of the shadow mask. In both cases we observe well separated sharp peaks attributed to single QD absorption (PC) and emission lines (PL). As a function of $V_B$ a Stark shift is observed, which is more strongy pronounced in the regime of PC. In PL (Fig. 4a) two lines at 1302.8 meV and 1307.4 meV ($V_B$ = 0 V) marked as $X^-_{PL}$ and $X^0_{PL}$ dominate the spectra. In the PC spectra (Fig. 4b) a single line, marked as $X^0_{PC}$, appears at 1303.6 meV ($V_B = -1.5$ V). Both these lines arise from the same QD as discussed below.

In PL, the two main lines $X^-_{PL}$ and $X^0_{PL}$ are separated by ∼4.6 meV. Both lines are observed even for very low excitation power of only ∼5 Wcm$^{-2}$ corresponding to the single exciton occupancy limit. Moreover, typical biexciton binding energies for these QDs are $\sim -3$ meV. In the regime of the PL, at low electric field, charging effects have been shown to play an important role on the characteristic features of the spectra. With increasing $V_B$ the band flattens and the electron levels of the QD are shifted below the Fermi-energy of the n-GaAs back contact. This results in successive single electron charging of the QD (discussed more in detail in Refs. [39, 41–43]). The data in Fig. 4a show the transition from the neutral to the single charged and the twofold charged exciton with increasing $V_B$. The charging of the QD is accompanied by discrete jumps in the emission energy due to few particle interaction of the exciton with an increasing number of electrons. Hence we can assign the two lines in the PL spectra for $V_B \leq 0$ V to the charged ($X^-_{PL}$) and neutral ($X^0_{PL}$) exciton state of the QD sepa-

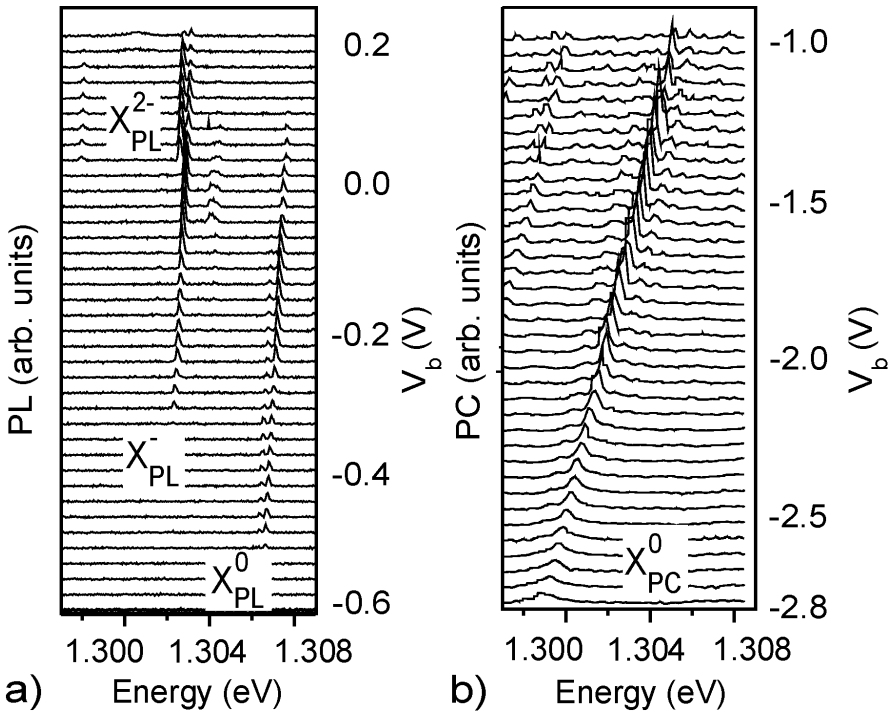


**Fig. 4** Photoluminescence (a) and photocurrent (b) spectra measured on a single QD photodiode as a function of the bias voltage $V_B$. In PC only the neutral QD is probed whereas in PL the $X^0$, $X^-$, and $X^{2-}$ states are created according to the external voltage. For direct comparisons between PL and PC data, the Stark shift and bias controlled charging of the QD have to be taken into account.

rated by the $X^-$ binding energy. In this sample, for $V_B \geq -0.35$ V the QD is already charged with one electron. Due to the statistical nature of the carrier capture process for non resonant excitation the $X^-$ and $X^0_{PL}$ lines coexist in the PL spectra of this sample for a certain range of $V_B$. To compare PL and PC data, without disturbing energy shifts due to many body effects, the uncharged QD ground state has to be considered. This is represented by the lines $X^0_{PL}$ and $X^0_{PC}$ in the PL and PC regime, respectively. The $X^0_{PL}$ line can be traced in bias voltage ranges of $-0.5$ V $\leq V_B \leq 0$ V. For $V_B \leq -0.5$ V $\tau_r$ exceeds $\tau_t$ and the PC regime is entered.

In the PC regime the electron states of the QD always lie far above the Fermi level of the n-GaAs back contact and the QD remains uncharged. To further study the influence of electric field on the uncharged exciton ground state the $X^0_{PL}$ line as a function of $V_B$ is presented in Fig. 4b. The PC signal can be observed in the voltage range from $-1$ V to $-2.8$ V. The magnitude of the PC saturates for $V_B \leq -1.3$ V (at a constant laser power of about 100 kWcm$^{-2}$). Under these conditions the experimentally observed PC peak magnitude is 140 pA ($X^0_{PC}$). This current corresponds to a generation rate of $10^9$ e–h-pairs per second. Without electric field the exciton lifetime in a QD $\tau_r$ is about 1 ns. For a generation rate of $10^9$ e–h-pairs per second and $\tau_r = 1$ ns, each QD would be, on average, occupied by a single exciton at a time. However, for a QD in electric field $\tau_T$ can be considerably smaller due to a reduced $\tau_t$: $\tau_T^{-1} = \tau_r^{-1} + \tau_t^{-1}$ and the statistical occupancy of the QD is well below one.

For a single QD, the reduction of $\tau_T$ with increasing electric field can be deduced from the PC line width. For increasing negative $V_B$ the PC line width becomes broader (Fig. 4). In the limit of high electric fields, the reduction of $\tau_T$ due to shorter $\tau_t$ is the main mechanism. $\tau_T$ can be estimated to be $\sim 0.3$ ps from the PC line width of about 1 meV at $V_B = -2.5$ V ($\Gamma\tau = \hbar/2\pi$). Assuming $\tau_T = 0.3$ ps, a statistical occupancy of the QD below $10^{-3}$ can be estimated from the PC magnitude. At the low field side, around $V_B \sim -1$ V, the PC amplitude quenches abruptly. Here the line width of 250 μeV is

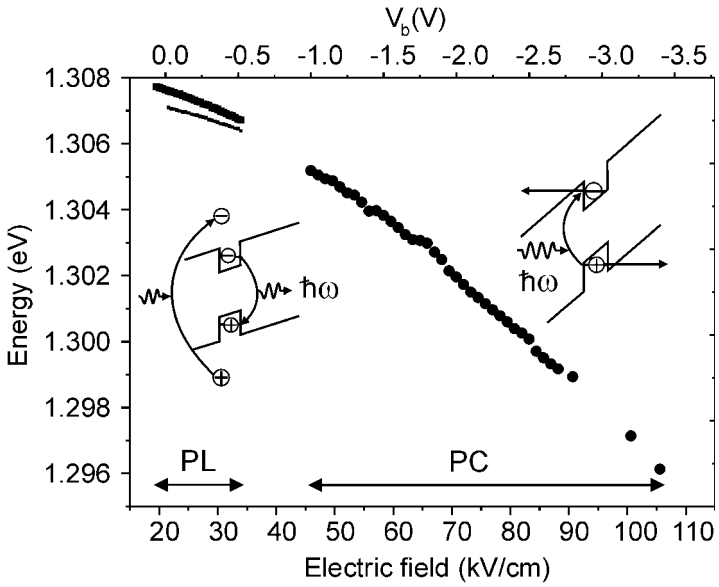


**Fig. 5** Line position of the neutral QD ground state as a function of the electric field measured in PL (main peak and satellite) and PC spectroscopy. The spectral shift due to the QCSE nicely continues in both regimes. The insets illustrate the different processes involved in PC and PL.

certainly not lifetime limited, but restricted by the experimental conditions. In the transition region between PC and PL the condition $\tau_T \sim \tau_r \sim 1$ ns is valid. The observed strong variation of the exciton lifetime from typical 1ns at zero electric field to below 1ps at 83 kV/cm can be used to directly tune the lifetime of the QD excitonic state.

To further compare the $X^0$ line position in PL and PC, the quantum-confined Stark effect (QCSE) has to be taken into account. The QCSE gives rise to a red shift of the QD ground state with increasing electric field $F$. The Stark shift continues monotonically over both regimes (see Fig. 5). This observation confirms, that one and the same QD is probed in both PC and PL experiments. Hence, such a monotonic behavior in absorption and emission spectra is expected only for an empty QD where renormalization effects are negligible. The field dependence of the $X^0$ transition energy $E^{X^0}$ can be described by the expression $E^{X^0} = E^{X^0[F=0]} + pF + \beta F^2$. Here, $E^{X^0[F=0]}$ is the transition energy at zero field, $p$ describes the permanent dipole moment and $\beta$ the polarizability of the QD-exciton. Taking PL and PC data into account the QCSE for this QD can be studied over a range of about 100 kV/cm. Using the PC data and the PL main peak we determined a nonzero dipole moment of $p = 8 \times 10^{-29}$ Cm. These values are in good agreement with the work of Fry et al. [49] who found $p = 7 \pm 2 \times 10^{-29}$ Cm for an ensemble of InAs QDs suggesting a localization of the electrons (holes) at the base (apex) of the QD.

We have seen now, that detailed insights into the charge distribution within a QD can be inferred form electric field tunable QD structures. For device applications, single QD photodiodes will inherently provide sharp resonant spectral sensitivity, a feature which is new in comparison to existing photodetectors based on semiconductor structures with higher dimensionality. Even more important is the fact, that this spectral response can be tuned by the QCSE. Within a limited energy range, a single QD photodiode provides therefore the function of a mesoscopic, electric field tunable spectrometer without any additional dispersive elements. Corresponding data are shown in Fig. 6 for excitation with various energies from a Ti:Sapphire laser. Even with the current devices it is possible to tune the detection energy over a range, which corresponds to more than $10\times$ the absorption linewidth. For applications in the nano-world it is further important to note, that the absorption volume of those devices is at the limit for a semiconductor detector, allowing for devices with the highest achievable spatial resolution.

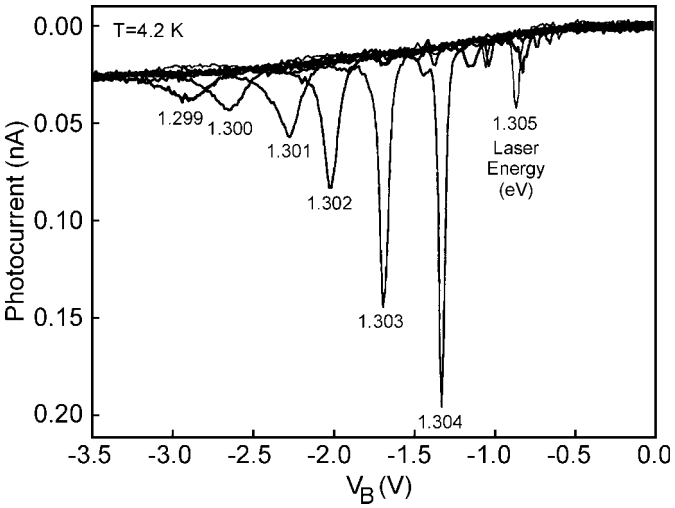


**Fig. 6** Photocurrent response (versus $V_B$) of a single quantum dot photodiode for different excitation energies.

### 2.2 A 2-level QD system with electrical contacts

So far we have discussed the single QD photodiode in the context of conventional semiconductor devices. Taking a more general look from fundamental physics, the single exciton state in a QD can be described within the general concept of a 2-level system. In this framework a single QD photodiode is essentially a single 2-level system with electric contacts, a configuration which has not been obtained so far on the basis of other 2-level system such as an isolated atom or spin. In the following we analyze the response of a single QD within the model of 2-level systems. This approach is valid within a limited energy range around the single exciton ground state of a QD, where only one particular dipole allowed transition is able to modify the occupancies of the two considered levels. In the present case the energetically lower level "0" corresponds to the empty QD ground state, the higher level "1X" to a single exciton occupancy. For resonant, incoherent cw excitation, one expects first an increase of the statistical 1X occupancy with increasing pumping power. In the high excitation limit, however, one expects saturation at a 1X occupancy of 0.5, since there are equal probabilities then for transitions from 0 to 1X and vice versa.

In Fig. 7a we present a series of PC spectra of a single QD photodiode for increasing excitation power. The dominating PC line results from the ground state absorption of the investigated QD. For further discussion we use the peak amplitude of the PC line as a measure of the QD ground state absorption at fixed electric field. Starting at a relatively low excitation level, the absorption line grows up significantly, but with increasing laser power we observe a saturation of the PC peak amplitude. Further absorption appears to be suppressed in the limit of high excitation. Additional background PC at high excitation intensities is probably due to additional non-resonant excitation of other QDs by stray light since all QDs are connected electrically in parallel. When a QD is occupied, its energy levels are subjected to a spectral shift (typically a few meV) due to renormalization effects [22, 42, 50, 51, 74]. Thus, no second absorption process can take place at the same excitation energy providing that the QD is occupied. Experimentally, we are able to monitor the occupancy of the QD quantitatively by measuring the PC as described above. A similar series of power dependent PC spectra have been taken for different bias conditions. They all exhibit a saturation of the PC amplitude, measured from the peak of the dominating PC line (at $\sim$1.3135 eV) with respect to the background PC. The experimental data are summarized in Fig. 7b. The saturation level of the PC amplitude shows a pronounced dependence on the electric field. At higher electric fields, the tunneling time is reduced and the QD returns more rapidly to its initial empty state. Therefore a higher absorption rate is possible, leading to a higher saturated PC. The saturation of the QD PC with increasing excitation power can be described by a fundamental rate equation model. In this model we concentrate on a specific

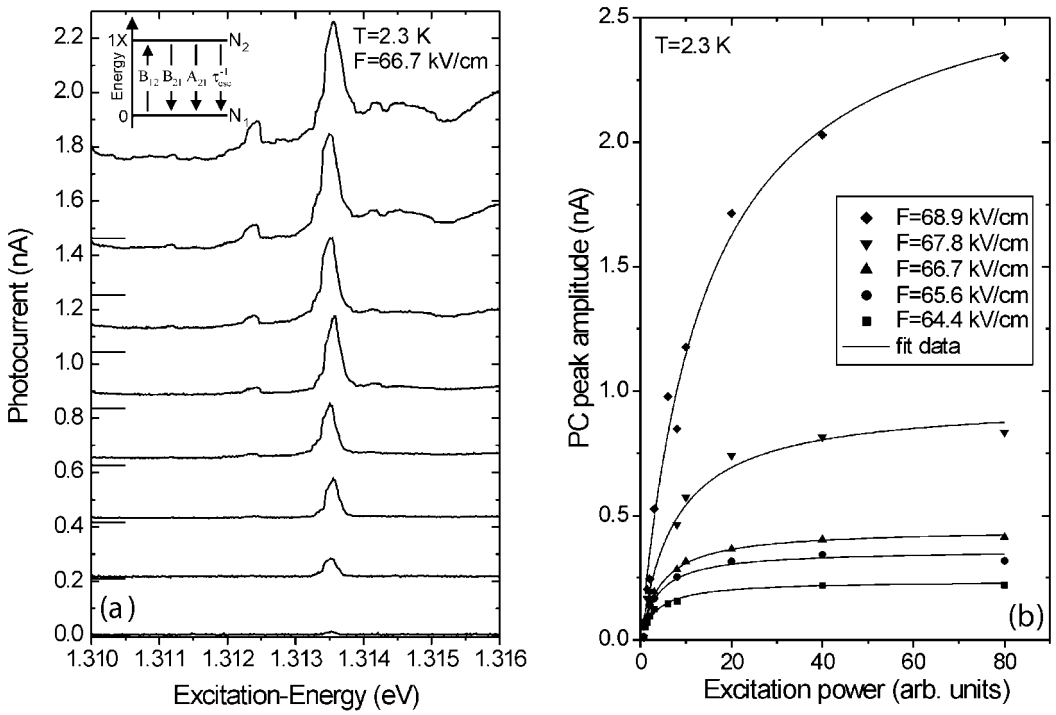


**Fig. 7** a) PC spectra of a single QD ground state under resonant excitation conditions. With increasing excitation power a saturation of the PC from the QD is observed. For each spectrum the zero PC line is indicated on the left. The inset shows a sketch of an excitonic 2-level system (see text). b) PC saturation as a function of excitation power for different bias conditions. For stronger electric fields a higher PC saturation value is observed. The experimental data are fitted by a specifically calculated function, based on the rate equation model described in the text.

QD ground state with an exciton occupation number $N$. The status of the QD is modeled in terms of a 2-level system. The QD is declared to be in level 1, if it is unoccupied, and in level 2 if it is occupied with one exciton. For these two levels we define two time-averaged occupation numbers $N_1$ and $N_2$, with values between 0 and 1 which sum to give unity $N_1 + N_2 = 1$. The underlying 2-level system is sketched in the inset of Fig. 7a. According to the theory of 2-level systems we consider the following rate equations:

$$\frac{\mathrm{d}N_1}{\mathrm{d}t} = A_{21}N_2 + B_{21}N_2\rho - B_{12}N_1\rho + \frac{N_2}{\tau_{\mathrm{esc}}}\,, \tag{1}$$

$$\frac{\mathrm{d}N_2}{\mathrm{d}t} = -A_{21}N_2 - B_{21}N_2\rho + B_{12}N_1\rho - \frac{N_2}{\tau_{\mathrm{esc}}}\,. \tag{2}$$

Here the well known Einstein coefficients ($A_{21}$, $B_{21}$ and $B_{12}$) correspond to spontaneous emission, stimulated emission and absorption, respectively. $\rho$ is the energy density of the radiation field. Further we include the escape process of the exciton out of the QD with a time constant $\tau_{\mathrm{esc}}$. To solve this system of rate equations we set $B_{12} = B_{21}$ [52] and introduce the factor $M$ reflecting the probability for the stimulated processes and we use $A_{21} = 1/\tau_r$, where $\tau_r$ is the radiative recombination time of the exciton. Furthermore the strength of the radiation field $\rho$ is expressed in terms of the excitation power $P$ of the radiation field. Due to the relation $N_1 + N_2 = 1$ we obtain

$$\frac{\mathrm{d}N_2}{\mathrm{d}t} = (1 - 2N_2)\,MP - \frac{N_2}{\tau_r} - \frac{N_2}{\tau_{\mathrm{esc}}}\,. \tag{3}$$

This rate equation describes the evolution of the QD occupation $N_2$. The last pair of terms in Eq. (3) represent the two exciton loss mechanisms of the QD; radiative recombination and escape of the exciton. The first term on the right hand side of Eq. (3) arise from the power dependent resonant creation and annihilation of the exciton. It reflects the balance between absorption and stimulated emission. Since the resulting effective change of the occupation depends on $(1 - 2N_2)$, we recognize that the absorption behavior of the QD is affected by the occupation of the dot itself. This property leads to the nonlinear power dependence and saturation of the PC. Returning now to the experimental data, we calculate the steady state occupation $N_0$ of the QD and use the escape term in Eq. (3) to obtain the resulting PC

$$I = e\frac{N_0}{\tau_{\mathrm{esc}}} = \frac{e}{\tau_{\mathrm{esc}}} \times \frac{P}{P + \frac{1}{2M}\left(\frac{1}{\tau_{\mathrm{esc}}} + \frac{1}{\tau_r}\right)} \,. \tag{4}$$

With this expression it is possible to fit the power dependence of the PC peak amplitudes in Fig. 7b (see full lines) with high accuracy. From Eq. (4) we obtain $I_{\mathrm{sat}} = e/2\tau_{\mathrm{esc}}$ as the high power saturation value of the PC. The tunnel escape time $\tau_{\mathrm{esc}}$ depends strongly on the chosen electric field. From a fit to the model we are able to obtain the tunneling escape time from the observed $I_{\mathrm{sat}}$. Since there are both electrons and holes in the QD, it is of interest which escape time (electron or hole) is relevant here. Since the tunneling time is strongly affected by the energy barrier and the effective mass of the carrier, electron and hole exhibit different tunneling times. After tunneling of the faster of the two carriers, there is still one carrier left in the QD and the absorption is still bleached due to renormalization [49]. After the second carrier has also tunneled out, the QD is again in its initial state and ready for the next absorption process. This demonstrates that it is the lifetime of slower tunneling carrier which controls bleaching and determines the value of the saturated PC. Equation (4) is used to calculate the carrier lifetime from the saturated PC. For saturation values of 2.78 nA at $F = 68.9$ kV/cm and 0.24 nA at $F = 64.4$ kV/cm one obtains a tunneling lifetime for the slow carriers of 29 ps and 330 ps, respectively.

An absolutely new optoelectronic functionality can be expected from a single QD photodiode, if it is driven by short laser pulses in the coherent regime. Recently coherent population oscillations, so-called Rabi oscillations [53] have been demonstrated in the exciton population of single QDs [31, 54, 55]. Low temperature dephasing times for excitons in self-assembled quantum dots ($\tau_p$) have been shown to exceed several hundred *ps*, allowing for sufficiently high numbers of coherent manipulations using ps pulses [35–37]. Tunneling on a timescale $\tau_t \leq \tau_p$ will lead to enhanced dephasing and limits the available time range for coherent interactions ($\tau_t$ accounts here to the first carrier which escapes from the QD – after the original excitation dephases). Safe conditions for coherent excitation can be however obtained by using *ps* pulses from a mode locked laser with a duration $\ll \tau_p$. Coherent optical excitations of a single QD photodiode are then expected to result in Rabi oscillations, which can be directly and directly measured via the photocurrent (PC). The principles of this idea are summarised by Fig. 8.

Optical excitation with a π-pulse results in the coherent generation of a single exciton, which is subsequently dephased and photoionized by tunneling. In the electric circuit this process is detected as separation of a single electron-hole pair and hence as a deterministic PC, which is equivalent to the flow of a single elementary charge $e$ through the diode. A repetitive optical excitation of a single quantum dot photodiode with π-pulses of frequency $f$ has therefore been predicted to result in a deterministic PC $I = f \times e$ [38]. A coherently driven single quantum dot photodiode is therefore an optically triggered single electron source, which offers, just like the related single electron turnstile device, single electrons (or holes) on demand. Both devices have the potential to deliver frequency controlled, deterministic currents according to $I = f \times e$. These concepts have been recently demonstrated experimentally for the first time [32–34]. An example is shown in Fig. 9 which shows the experimentally deduced photocurrent resoponse as a function of the amplitude of the coherent excitation pulse. Clear damped Rabi oscillations are observed with the maximum photocurrent of $\sim 12.6$ pA upon application of a π-pulse close to expectations for the $f = 82$ MHz laser repetition frequency.

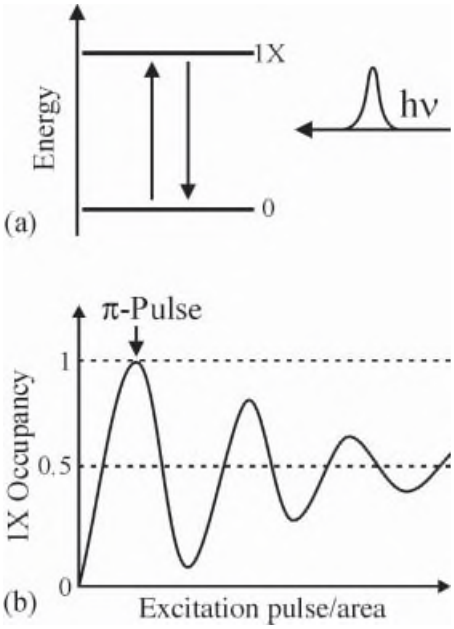


**Fig. 8** a) 2-level system corresponding to the quantum dot ground state 1X in a photodiode with resonant, pulsed excitation. b) Rabi-oscillations in the 2-level system versus the excitation pulse area in the presence of weak decoherence. Application of a π pulse results in a 1X occupancy close to unity.

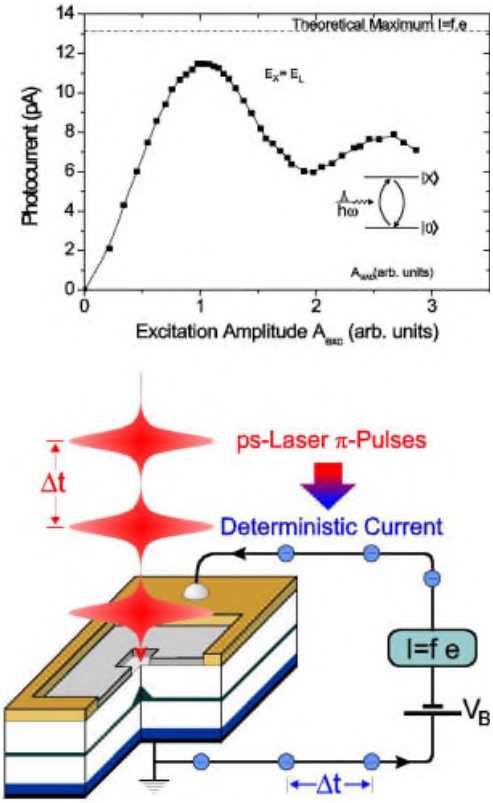


**Fig. 9** a) Experimentally measured PC response of the neutral exciton as a function of the excitation pulse area showing damped Rabi oscillations. Following excitation with a π-pulse the PC amplitude is more than 90% of the theoretical maximum as discussed in the text. b) Operation of a single dot photodiode as a deterministic current source: following each excitation with a π-pulse a single elementary charge flows through the external circuit.

Using circularly polarized excitation a single QD photodiode has the further the potential to provide deterministic streams of spin polarized charges, with potentially strong implications in quantum information processing.

## 3 Spectroscopy of coupled InGaAs quantum dots with tunable electronic states

### 3.1 Sample design and experimental setup

Our approach towards a study of coupled QDs is the use of double layers of self-assembled QDs separated by a thin barrier. For a systematic control of the electronic coupling strength of QD states in the two layers, three different electric field tunable $n-i$ structures were grown by molecular beam epitaxy. The samples contain two layers of $In_{0.5}Ga_{0.5}As$ QDs (each consisting of 8 ML $In_{0.5}Ga_{0.5}As$) separated by spacer layers of 7 nm, 10 nm and 13 nm, respectively. The QD molecule layers are

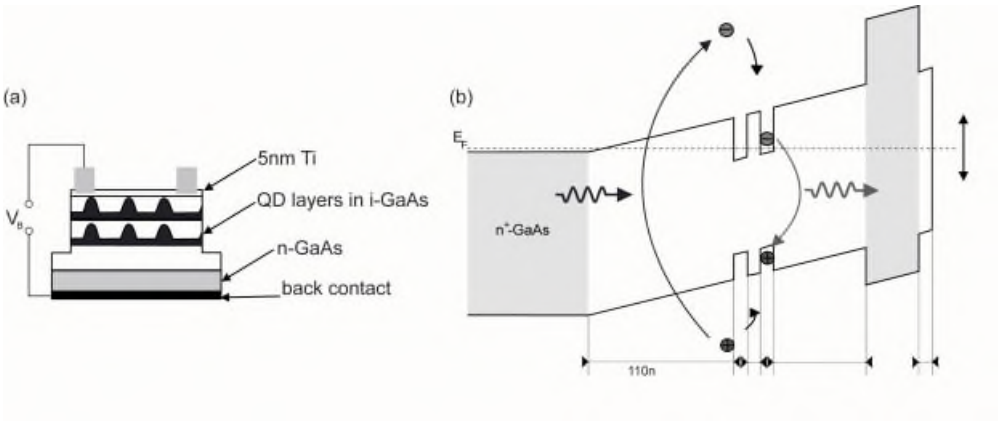


**Fig. 10** a) Schematic sample structure: two layers of QDs embedded in the intrinsic region of a photo-diode. b) Band diagram of the samples of our study.

embedded in an intrinsic GaAs region, 110 nm above an $n-$doped GaAs layer (doping level $5 \times 10^{-18}$), which also acts as a back contact. This thick barrier between the QD layers and the dopants prevents significant tunnel injection of electrons in the QDs. The spacer layers are chosen thin enough to achieve self-aligning of the QDs in the two layers, which is verified by atomic force microscopy studies on cleaved [110] facets of the 13 nm sample. The QD layers are followed by 70 nm GaAs, a 40 nm wide $Al_{0.3}Ga_{0.7}As$ blocking barrier layer and a 10 nm GaAs cap layer to prevent oxidization of the sample surface. Then 5 nm Titanium is evaporated as a semitransparent Schottky gate acting as the top electrode. In the following, the samples are referred to as the 7 nm-, 10 nm-, and 13 nm-sample resembling the thickness of the spacer layer. The samples are processed as photodiodes as depicted schematically in Fig. 10(a).

Figure 10(b) shows a schematic drawing of the band diagram of the samples of our study. The internal electric field can be tuned by applying an external bias $V_B$ between the Schottky gate and the back contact. Specifically, tuning the internal electric field across the stacked QDs enables us to adjust the relative energetic position of the electronic states in the upper and lower QD with respect to each other. The thickness of the intrinsic region of the diode is chosen in a way to achieve resonance of the QD single particle states for moderate electric fields $(60; 30\,\mathrm{kV/cm})$. As a result, photoluminescence (PL) experiments can be performed and the tunneling escape of carriers out of the QDs can be neglected in comparison to radiative recombination ($\tau_r \simeq 1\,\mathrm{ns} > \tau_{\mathrm{tunneling}}$ see [40]).

The experiments are performed at liquid Helium temperature and free electron–hole pairs are photo-generated by non-resonant excitation at 632.8 nm. The luminescence generated is dispered using a 0.25 m spectrometer and a liquid nitrogen cooled Germanium photo-diode.

### 3.2 Results and discussion

PL spectra obtained from the three samples are plotted as a function of the applied external bias voltage $V_B$ in Fig. 11 (left panel) as a greyscale plot. The onset of the PL signal for all samples is found for a forward bias of $+0.5\,\mathrm{V}$. For smaller bias the carrier capture quenches because of the increasing internal electric field and PL is not observed. Both samples exhibit a main luminescence peak (labeled "EP" in Fig. 11) originating from the upper layer of QDs since it is the predominant PL signal over the whole bias region. The shift to higher energies of this main luminescence EP originates from the Quantum Confined Stark Effect. Since the InGaAs coverage for both QD layers was nominally identical and the thin spacer layer preserved the strain field for the growth of the second layer (leading to self-alignment) the Stranski–Krastanov growth of the QDs in the second layer commences at a lower critical thickness. This leads to larger QDs with lower lying electronic states com-

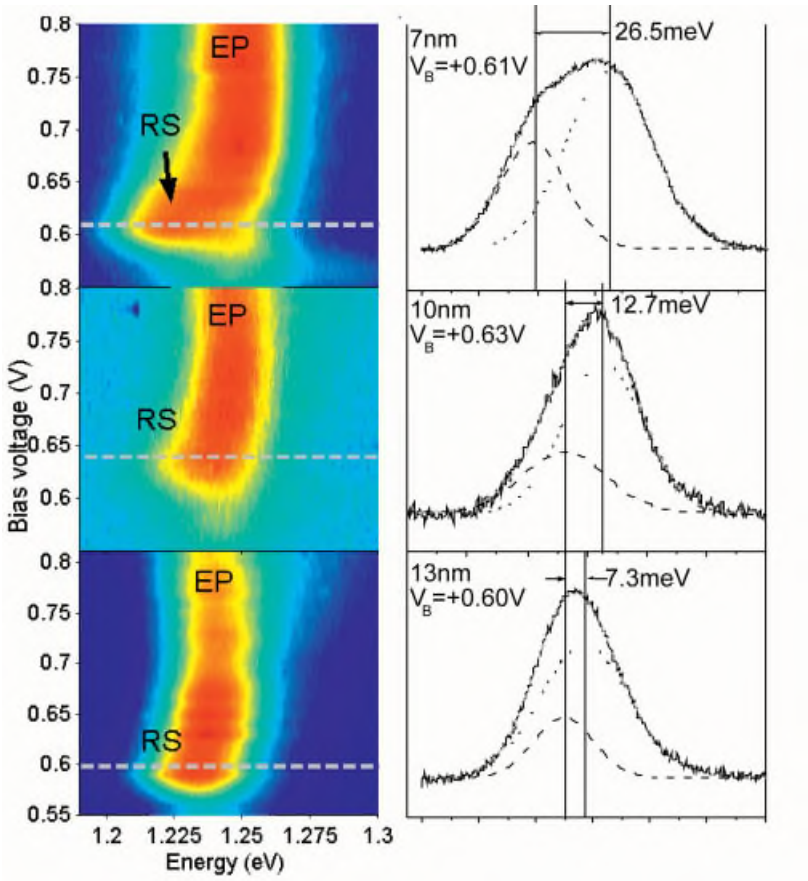


**Fig. 11** Left panel: greyscale representation of the PL spectra as a function of the applied external bias for the 7 nm- (top) 10 nm- (middle) and 13 nm-sample (bottom). All spectra show the ensemble peak (EP) and a prominent red-shifted shoulder (RS), which appears only in a small bias region. This red-shifted shoulder is most prominent for the 7 nm-sample. Right panel: spectra observed for different bias voltages $V_B$ indicated by the dashed lines in the greyscale plots. The dashed and dotted lines are fitted curves for the two peaks. Apparently the splitting of these lines decreases with increasing spacer thickness.

pared to the lower QD layer due to reduced lateral confinement [25, 26]. The results of our luminescence measurements suggest that the QDs in the upper layer are energetically preferred for holes to relax into these QD states since no PL of the lower QD layer is detected.

Comparing the bias dependent PL spectra obtained from the samples we observe a very pronounced red shoulder (labeled "RS" in Fig. 11) which is observed for all biases but becomes very pronounced over a narrow range of $V_B$. This resonance occurs at $V_B = +0.61$ V, $+0.63$ V and $+0.60$ V for the 7 nm- 10 nm- and 13 nm-samples, respectively and weakens significantly at smaller and larger biases as shown in Fig. 13. Selected PL spectra obtained from each sample for $V_B \sim 0.6$ V are depicted in the right panel of Fig. 11 in more detail. The spectra obtained from each sample at these bias voltages enables us to identify two distinct, inhomogeneously broadened PL peaks. We performed least square fits of the PL lineshape using two Gaussian peaks in order to accurately obtain a measure of the energy separation of the two peaks. For the 7 nm-sample, the best fit was obtained using two Gaussian peaks of widths of 27 meV (RS) and 37 meV (EP), separated by $(26.5 \pm 0.4)$ meV. The splitting then exhibits a pronounced decrease for the 10 nm- and 13 nm-sample with values of $(12.7 \pm 0.8)$ meV and $(7 \pm 2)$ meV, respectively. The specified errors of the splittings are the variance

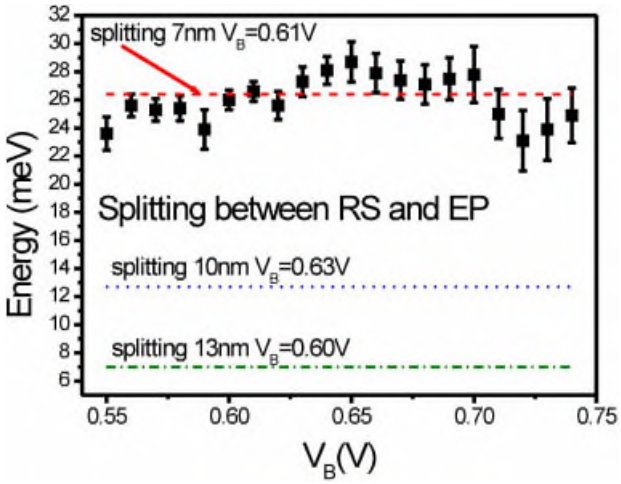


**Fig. 12** Energetic splitting of RS and EP as a function of applied bias. No prominent bias dependency is observed. The splitting varies around $(26.1 \pm 1.2)$ meV. The horizontal lines indicate the splittings obtained for the bias voltage where the most pronounced RS luminescence for the respective spacer thicknesses is observed.

of several fits of different spectra obtained at the respective biases. The errors of the single fits are smaller by a factor of 10 and are therefore negligible.

Due to this bias and spacer thickness dependence, we attribute the red shoulder RS to the formation of a strongly coupled electronic state. In this case we expect the appearance of an additional PL line due to mixing of the electronic states in the upper and lower QDs in analogy with the formation of bonding and antibondng molecular orbitals. Since our measurements are performed on large ensembles of QDs we observe the red shoulder over a relatively small bias region parallel to the main ensemble luminescence. We can exclude possible attribution of RS due to charging effects since this would lead to the EP disappearing and RS remaining at increasing bias.

The energy splittings between RS and EP is shown in Fig. 12 as a function of the applied bias. The splitting is approximately constant over the whole bias region with small fluctuations. Statistical analysis gives an average splitting of $(26 \pm 2)$ meV. For further understanding of the bias dependency of the PL of the 7 nm-sample the ratio of the peak areas of the fitted Gaussian peaks for RS and EP is depicted in Fig. 13 as a function of the bias voltage. At the onset of the PL emission, the ratio is 0.3. It then increases before reaching a maximum of 0.74 at $V_B = 0.61$ V. For increasing bias this ratio decreases and remains almost constant at a value of 0.4. This analysis is not possible for the 10 nm- and 13 nm-sample due to the smaller splitting energies which leads to unreliable fit results for the off-resonance case although the same qualitative behavior is obvious from the results of Fig. 11. This ratio qualitatively reflects the portion of the two QD ensembles whose electronic states are in resonance.

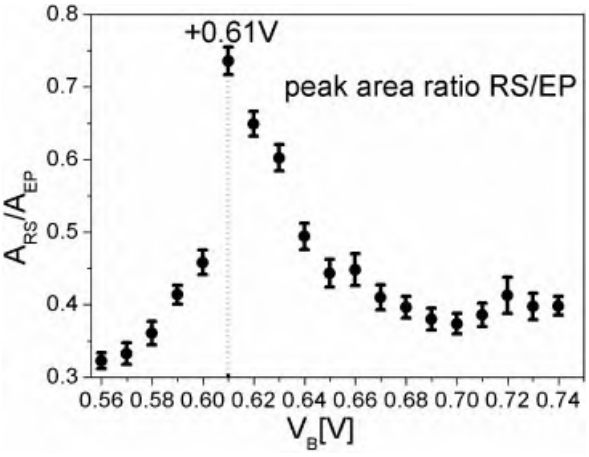


**Fig. 13** Ratio between the areas of the fitted peaks RS and EP for the 7 nm sample as a function of the applied bias voltage. One can clearly see a resonance at $V_B = 0.61$ V where the maximum energetic overlap of both QD ensembles was reached.

Due to the non-uniformity of the QD ensembles in both layers for the whole bias region scanned in our experiments certain subsets of the two QD ensembles are in resonance and therefore show coupling behavior. As a result, the ratio of the peak areas is non-zero over the entire bias range. The pronounced appearence of RS indicates the existence of a large subset of QD pairs with similar coupling behavior.

The energetic splittings observed experimentally are in fair agreement with recent theoretical perdictions for the single-particle energies in coupled QDs in the work of [57]. Two coupled spherical InGaAs QDs of the same size are modelled with a cylindrical Gaussian compositional profile layed basis. For the average Indium content 66%, for the height 0.92 nm and for the radius 24.9 nm are adapted form single layer QD PL data. In contrast AFM studies on InGaAs QDs grown under nomially identical conditions in the same MBE machine as the QDs studied in the present work show that these QDs are elongated along the $[1\bar{1}0]$ direction due to lower adatom mobility along the $[110]$ direction [58]. There are also uncertainties concerning the exact shape and morphology of our QDs. For a reasonable comparision, we assume that the height of our QDs is reduced during the overgrowth by about 40% which leads to a height of 4 nm for our buried QDs using 7 nm as an average value for the height of uncapped QDs. Using this assumption, splittings between the electron *s* state in a single QD and the coupled *s* state of even parity (e.g. binding state) in two stacked QDs of 21 meV, 8 meV and 3.5 meV for spacer layer ticknesses of 7 nm, 10 nm and 13 nm, respectively, have been predicted [57]. Taking into account the structural uncertainties mentioned above, our experimentally obtained splittings are in good agreement, supporting the identification of the PL features presented here. In summary, we have used PL spectroscopy to investigate coupling effects between electron states in stacked InGaAs/GaAs QDs separated by GaAs spacers of 7 nm, 10 nm and 13 nm. The coupling strength and the relative energetic position of the carrier states was controllably varied by changing the static electric field applied parallel to the QD growth axis. The influence of the electronic coupling decreases strongly with increasing spacer thickness between the stacked QDs and the experimentally obtained coupling strengths are in good agreement with theoretical predictions. An extension of this work concerning spectroscopy of individual QD-molecules is currently in progress.

## 4 Two-color femtosecond spectroscopy of blue-shifted InAs/AlGaAs quantum dots

### 4.1 Blue-shifted InAs/AlGaAs quantum dots

We study self-organized InAs quantum dots grown on an $Al_{0.3}Ga_{0.7}As$ layer capped with two monolayers of GaAs [59]. This procedure allows for the growth of high-quality quantum dots with a large confinement potential. As depicted in Fig. 14, the as grown sample exhibits a ground state luminescence around 1.1 eV (grey line), slightly blue-shifted as compared to the standard InAs islands embedded in GaAs. After an annealing step of 160 s at a temperature of $T = 1000$ K, the low temperature luminescence is found at photon energies around 1.42 eV (black line in the upper part of Fig. 14). This drastic blue-shift is attributed to an interdiffusion of aluminum into the InAs islands. The luminescence linewidth of 55 meV points towards a broad distribution of sizes and material compositions within the quantum dot ensemble. Additional prominent luminescence peak are found above 1.5 eV indicating the energetic position of both the band edge of the GaAs substrate and the wetting layer surrounding the InAs islands.

To overcome the problem of inhomogeneous broadening of the quantum dot ensemble, single zero-dimensional structures are to be isolated on the sample. To this end, the InAs layer is deposited without rotating the wafer during the growth procedure. Therefore, regions with a low quantum dot density may be found on the sample. Additionally, nanometer scale aluminum shadow masks are deposited on the wafer as described in Section 2. The lower part of Fig. 14 depicts the photoluminescence detected through a 350 nm aperture. Narrow emission lines between photon energies of 1.40 eV and 1.43 eV are clearly identified and correspond to the ground state luminescence of a few quantum dots. As a consequence, this material system allows for optical experiments in a spectral window where femtosecond Ti:Sapphire lasers and sensitive Si-detectors may be operated.

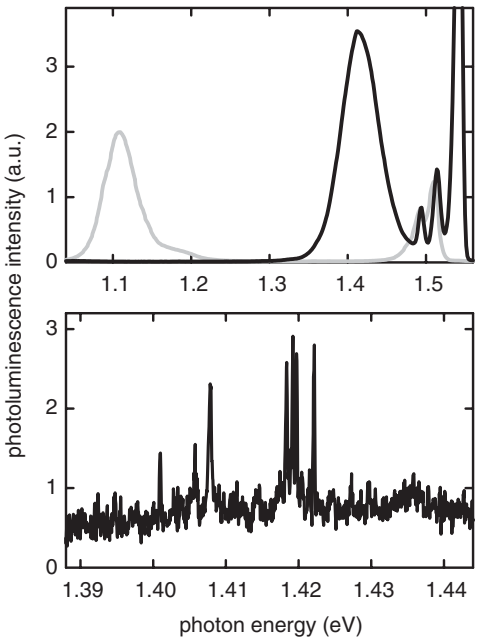


**Fig. 14** Upper Part: Photoluminescence of a large ensemble of InAs/AlGaAs quantum dots at a lattice temperature of $T_L = 4.2$ K: as grown (grey line) and after the annealing procedure described in the text (black line). The sample is excited with a cw laser at 1.96 eV. Lower part: Photoluminescence observed through a 350 nm shadow mask at the same experimental conditions. Note the different scale of the abscissa.

### 4.2 Experimental concept

Our experimental setup relies on a special two-color femtosecond Ti:sapphire laser that provides two independently tunable, perfectly synchronized laser pulses with durations between 13 fs and 120 fs [60]. The additional implementation of dispersion-free pulse shapers [61] allows for the generation of laser pulses with a smaller bandwidth of $\Delta E \geq 1.5$ meV and a corresponding transform-limited duration of up to 1 ps. The temporal separation of the pulses is adjusted via a variable delay line. The sample is mounted on the cold finger of a liquid helium microscope cryostate operated at lattice temperatures of $T_L \geq 3$ K. The laser light is focussed onto the sample employing a dispersion-free reflecting mirror objective with a high numerical aperture of NA = 0.4 mounted on piezo transducers outside the cryostate. An aspheric lense on the rear side of the sample is used to collect both the transmitted laser light and the sample luminescence. After passing a monochromator (typical spectral resolution: 1 meV) the light is analyzed with a single photon counting system or a silicon avalanche diode for luminescence or transmission experiments, respectively.

### 4.3 Results for an ensemble of quantum dots

First, the properties of blue-shifted InAs quantum dots at a lattice temperature of $T_L = 3$ K are studied with the experimental method of time-correlated luminescence. Taking into account the size of the laser spots on the sample and the density of quantum dots on the wafer, the number of zero-dimensional structures contributing to the observations is estimated to be $N \approx 1000$.

A first 100 fs laser pulse centered at a photon energy of 1.47 eV resonantly generates localized electron–hole pairs within the quantum dots (interband transitions (1) in Fig. 15). After a certain delay time $t_d$, a second pulse (probe) with a duration of 200 fs and a variable central photon energy is used to analyze the transient modifications of the sample. To this end, information on the absorption of the probe laser pulse is obtained via the emission changes at the ground state luminescence of the InAs islands at 1.355 eV.

First, we discuss the case of resonant carrier generation in the wetting layer or the GaAs substrate via the interband transitions (2) and (3) in Fig. 15. For this case, the experiment is sensitive especially to the occupation of the quantum dots. Specifically, electrons and holes generated in the wetting layer

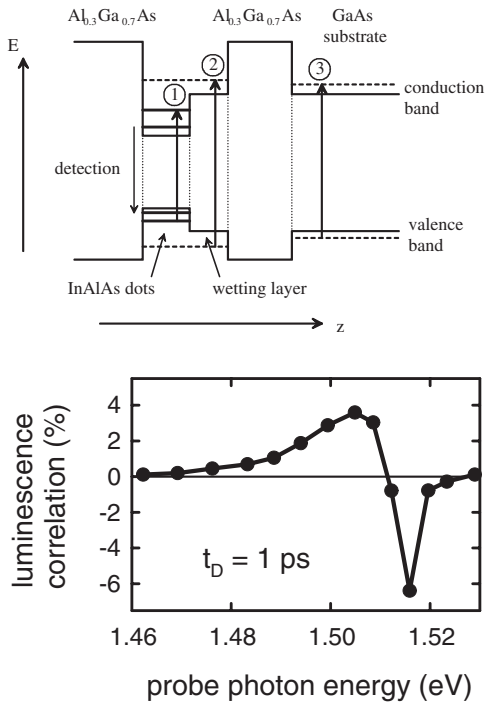


**Fig. 15** Upper part: schematic band diagram of the quantum dot sample. The interband transitions employed in the experiment are denoted with (1), (2), and (3) and explained in the text. Lower part: time correlated luminescence for various probe photon energies observed at a delay time of $t_D = 1$ ps after exciting the quantum dots with a 100 fs pulse centered at 1.47 eV. The lattice temperature is $T_L = 3$ K and the sample luminescence is detected at 1.355 eV with an energy bandwidth of 10 meV.

may scatter into the quantum dots efficiently only if the energy levels are unoccupied. Correspondingly, a negative luminescence change is found at probe photon energies of 1.516 eV (compare lower part of Fig. 15) after excitation with the pump pulse. As may be seen from the topmost curve in Fig. 16, this transient modification decays on a timescale of 100 ps related to the carrier lifetime in the quantum dots.

Surprisingly, the time-correlated luminescence signal decreases rapidly for larger probe photon energies in Fig. 16. Apparently, the capture process of uncorrelated electron–hole pairs from the wetting layer into the quantum dots differs qualitatively from the case of excitonic states near the band edge.

A distinctly different behavior is found when the probe pulse generates electron–hole pairs within the quantum dots (generation of localized carriers via the interband transitions (1) in Fig. 15). As may be seen from the time-correlated luminescence for the probe photon energies of 1.505 eV and 1.489 eV in Fig. 16, an enhanced probe-induced luminescence is found after excitation with the pump pulse. This finding reflects the modifications of interband transitions (1) in Fig. 15 due to the carrier generation in the dots: occupying self-organized quantum dots with electron–hole pairs generally results in an energetic red-shift of interband transitions of several meV due to Coulomb renormalization [22, 62]. As a consequence, a larger number of interband transitions is resonant with the probe pulse after carrier injection. The picosecond dynamics of the time-correlated luminescence signal is related to an intra-quantum dot relaxation mechanism, e.g. by polar optical scattering of carriers into energetically lower quantum dot states. However, it is difficult to obtain a more precise understanding of the relaxation mechanisms since a large, inhomogeneously broadened ensemble of quantum dots contributes to the signal.

### 4.4 Results on isolated quantum dots

In order to obtain a more detailed picture of the dynamical properties of single self-assembled quantum dots, we now turn to the investigation of shadow masks that isolate systems of a few zero-dimensional InAs islands on the specimen. Figure 17 depicts the photoluminescence spectra of a 350 nm aperture detected with an energetic resolution of 2 meV for various excitation powers. Free carriers

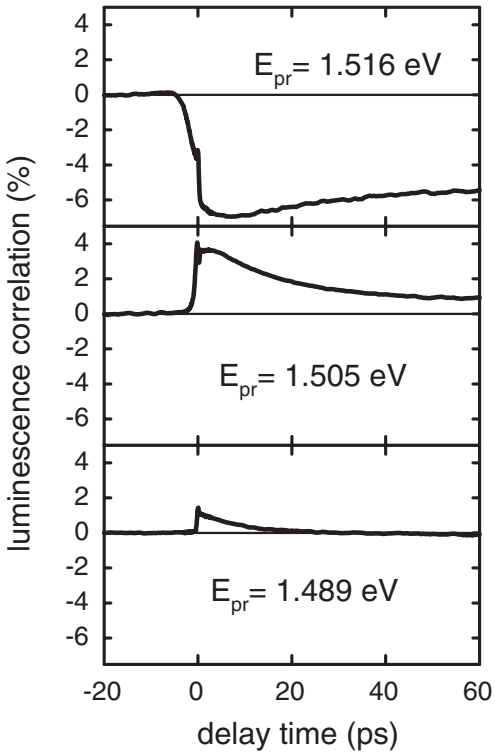


**Fig. 16** Time-correlated luminescence as a function of delay time for various probe photon energies $E_{\rm pr}$ given in the figure. The sample is excited with a 100 fs pulse at a photon energy of 1.47 eV. The lattice temperature is $T_L = 3$ K.

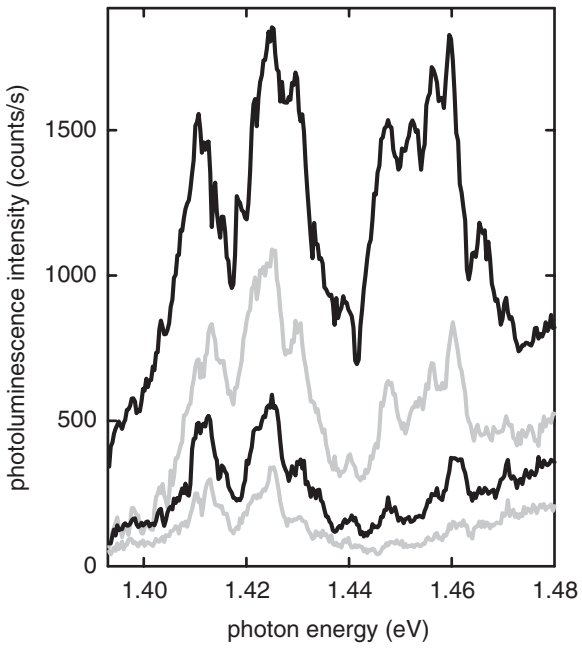


**Fig. 17** Photoluminescence detected through a 350 nm aperture at a lattice temperature of $T_L = 4.5$ K. The specimen is excited with a cw laser at 1.96 eV. The different curves correspond to various excitation powers: 50 W (upper black line), 25 W (upper grey line), 12 W (lower black line) and 6 W (lower grey line). The spectral resolution is set to 2 meV.

are generated with a cw laser at 1.96 eV at a lattice temperature of $T_L = 4.5$ K. As may be seen from the spectra for low excitation powers, the emission from the nanoaperture is dominated by the ground state luminescence of approximately five quantum dots around 1.42 eV. The intensity of these lines is found to increase slightly sublinearly with the excitation power indicating a beginning saturation of the quantum dot occupation. In contrast, the intensity of the luminescence lines found at photon energies between 1.446 eV and 1.462 eV exhibit a clearly superlinear increase with the excitation power. Apparently, these features correpond to the emission of excited states of the quantum dots under the nanoaperture. Our findings indicate an energetic separation of the first excited state transition in the order of 40 meV which is in agreement with studies on conventional self-organized quantum dots [63].

A comparable aperture with a diameter of 2 μm and a corresponding number of quantum dots in the order of $N \approx 100$ is now studied in a two-color femtosecond transmission experiment. In contrast to the results of the time-correlated luminescence experiment described above, very low signal levels are expected due to the weakly absorbing quantum dot monolayer. However, a transmission experiment utilizing broadband probe pulses allows for studies with optimum energy-time uncertainty.

The specimen is excited with a 300 fs pump pulse of a narrow bandwidth of 5 meV centered at 1.462 eV. As a consequence of this choice, only a subensemble of $N \approx 10$ quantum dots is expected to be excited via resonant absorption into the first excited excitonic states. The broadband 50 fs probe pulse is centered at 1.43 eV and encompasses the interesting spectral window around the ground state transition energies of the selectively excited quantum dots. The transmitted probe light is spectrally

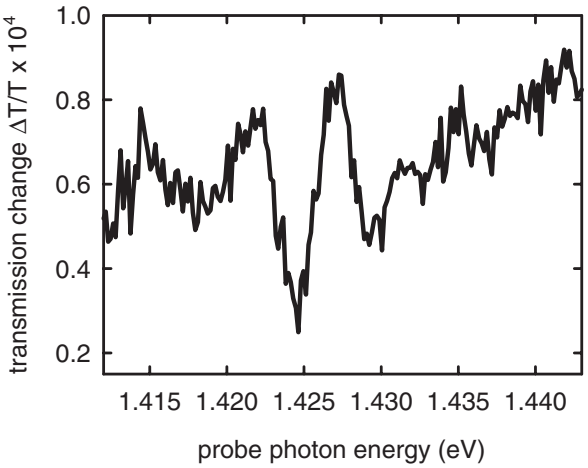


**Fig. 18** Spectrally resolved transmission changes detected through a 2 m aperture for a delay time of $t_D = 1ps$ after excitation with a 300 fs pulse centered at 1.462 eV. The lattice temperature is $T_L = 4.5$ K.

dispersed with a resolution of 1.5 meV. Figure 18 depicts the spectrally resolved transmission changes obtained for a delay time of $t_D = 1$ ps. As the most striking feature, a dispersive structure is well resolved at 1.424 eV, red-shifted by 38 meV with respect to the excitation. This observation points towards a slight redshift of the ground state transition energies of the occupied quantum dots due to Coulomb renormalization. Comparable energetic shifts have been found in photoluminescence experiments [22, 62] as well as in theoretical simulations [64, 65]. In future experiments, these energetic shifts of an excitonic state may be exploited in quantum-correlated operations with two interband transitions serving as qubits [37].

In conclusion, we have studied self-organized InGaAs/AlGaAs quantum dots with different methods of femtosecond spectroscopy. Investigating a large ensemble of InAs islands in a time-correlated luminescence experiment, a picosecond relaxation mechanism within the quantum dots is found. The additional implementation of nanoapertures on the sample allows to study systems containing only a few zero-dimensional objects. The energetic separation of the first excited excitonic transition and the ground state is found to be approximately 40 meV paving the way for ultrafast switching operations, e.g. implementations of a quantum-controlled NOT gate which may be addressed on a femtosecond timescale. In the first realization of a two-color femtosecond transmission experiment on isolated quantum dots, we observe an energetic red-shift of the ground state transition energy after occupation of the first excited state. As a consequence, this technique may soon demonstrate ultrafast studies on single self-assembled quantum dots and coherent manipulations in a system of two excitonic qubits.

## 5 Optical memory structures based on InGaAs quantum dots

### 5.1 Overview

We have already discussed in previous sections that measurements performed on large ensembles of self-assembled QDs typically reveal a strongly inhomogeneously broadened PL linewidth in the range of several $\sim$10 meV. This is often considered to be a significant obstacle on the path towards the full exploitation of QD-based devices. However, in this section we describe a novel application in which inmogeneous broadening may actually be advantageous as it enables frequency selective optical excitation of a small subset of QDs within the ensemble. In 1995 Muto [66] suggested that such an inhomogeneously broadened ensemble of absorbing centers may have potential applications as wavelength domain optical data storage media. In order to develop such technologies, device concepts have to be established that allow for efficient electrical or optical detection of optically written information. Whilst optical writing has the clear advantage of opening the wavelength domain for information storage, the resulting excitations (excitons) are relatively short lived (typically 1 ns in a direct gap III/V semiconductor) and electrically neutral. For memory applications, these limitations can easily be over-

come by implementing a mechanism for charge separation based on electric field induced ionization of excitons on timescales shorter than the radiative lifetime. The concept of field ionization and charge separation has been widely used in semiconductor devices over the last decades. Among the most important devices in this category are photodiodes and CCD detectors. More recently, related strategies have been proposed for 2-dimensional structures, such as charge separation in coupled quantum wells [67] and lateral charge separation in single quantum wells by electric fields or surface acoustic waves [68]. However, from a more general perspective a number of important quantum properties of the incident photons (polarization, frequency, coherence and spatial absorption position) are irreversibly lost by applying such schemes. Since the advent of high quality semiconductor QD systems, some of these fundamental limitations can now be overcome. Whereas the associated improvements of the decoherence times are in particular important in the context of quantum computing, [29, 30] some other basic properties of QDs have a more direct impact on memory devices. The most basic property of a QD is certainly its discrete density of states and, therefore, a discrete absorption and emission spectra that allow basically for energy conservation during an absorption-emission (write – read) cycle. The temporal transfer of one of the charge carriers out of the QD, required for the realization of long storage times, does not destroy the energetic information deposited during the absorption process, providing that the second carrier remains in the QD. Subsequent back-transfer of the ionised carrier species into the dot reestablishes an exciton in the groundstate of the same QD which can emit from the same quantum mechanical environment at the energy of absorption. The localization of a carrier in a defined nano-environment is therefore an important concept, which applies naturally also to spatial information, and – under suitable conditions concerning the spin lifetime – also to spin and hence optical polarization.

From these basic considerations, it seems therefore most promising to implement optical write and read in order to extract maximum benefit out from the underlying QD hardware. First exploratory investigations in this field were concentrated however on optical write and electric readout, an approach which seems to make sense in view of the challenges invoked in this new theatic area. Yusa and Sakaki demonstrated an optically gated FET, which incorporates a layer of InAs QDs [69]. The operation of this device was attributed to the preferential trapping of nonresonantly photo-generated holes in a QD layer. Finley et al. have extended this approach to conditions of resonant excitation in the region of the ground state of the QD ensemble [70]. Shields et al. have demonstrated a scheme of electric readout in considerably smaller FET structures, which allows to monitor discrete charging events of single QDs in the FET transport [71] and a first demonstration of optical readout was presented by Lundstrom et al. employing electric field induced charge transfer in both directions between a QD and a strain-induced potential minimum in an adjacent QW [72].

### 5.2 QD optical memory structure with electrical readout

In this section we will concentrate first on a more detailed description of an FET memory structure designed for optical write and electric readout. The concept of electric read out is based on electrostatic interaction between a chargeable QD and a 2DEG. The introduction of net charge into the QDs will have two different effects on the electron system; a change of both the carrier concentration and mobility by introducing additional Coulomb scattering. The band diagram of the device is shown in Fig. 20 for different operating conditions. As important ingredients the device contains a two-dimensional electron gas (2DEG), a layer of self-organized InAs quantum dots, and a back contact. The device is designed to store electrons in the QD layer, with the charging condition being monitored via the resistance of the 2DEG. The device was grown on a [100]-oriented semi insulating GaAs substrate and consisted of the following layers: A 500 nm p-GaAs back contact ($p = 2 \times 10^{18}$ cm$^{-3}$) followed by a 240 nm undoped GaAs spacer. This was followed by 2.25 ML of InAs grown at 530 °C (QD layer) and a composite tunnel barrier consisting of 30 nm undoped $Al_{0.3}Ga_{0.7}As$ and five periods of a 2 nm(AlAs)/2 nm(GaAs) superlattice. After this a 10 nm thick $In_{0.1}Ga_{0.9}As$ electron channel was grown followed by a 40 nm wide modulation doped $Al_{0.3}Ga_{0.7}As$ barrier. The modulation doping was

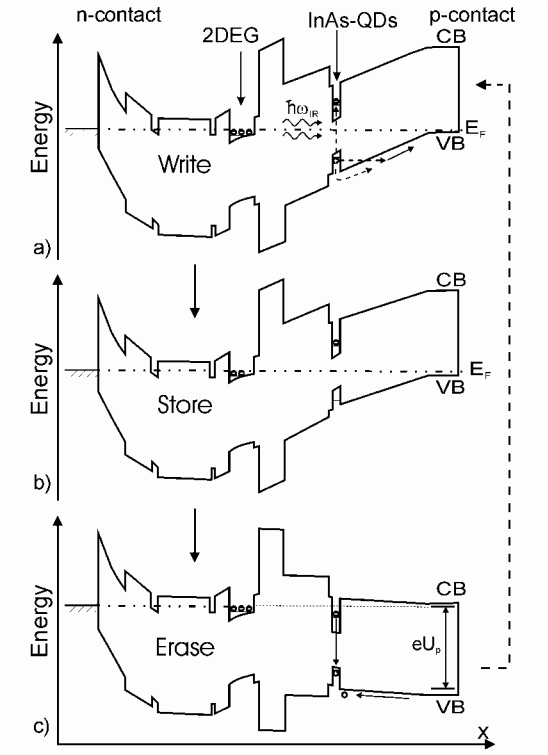


**Fig. 19** Schematic band diagram and operating principle of the optical memory structure. a) Write cycle: Optical excitation of e–h pairs in the QD-layer, followed by hole escape by tunneling. b) Store condition: Electrons remain trapped in the QD-layer. c) Erase cycle: $V_{pn}$ is switched to forward bias condition. Holes drift to the QD-layer followed by radiative recombination with the stored electrons.

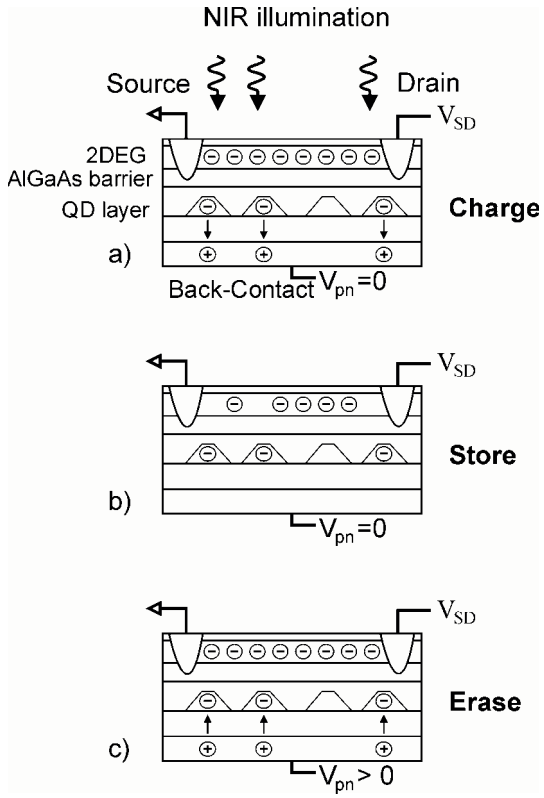


**Fig. 20** Schematic device structure and operating principle of the optical memory structure. a) Write cycle: Optically excited e–h pairs are separated in real space, electrons remain stored in the QDs. b) The stored negative charge acts electrostatically on the 2DEG and causes depletion, which can be monitored in the source–drain resistance. c) Application of a reset pulse causes hole drift to the QD-layer followed by radiative recombination with the stored electrons.

incorporated into two 1.5 nm $\delta$-doped ($2 \times 10^{12}$ cm$^{-2}$) GaAs quantum wells. Finally, the structure was capped with 10 nm of n-doped ($4 \times 10^{18}$ cm$^{-3}$) GaAs. The wafers were processed into a Hall bar geometry using standard optical lithographic techniques and separate ohmic contacts were established to both the 2D electron channel and the p-type back contact. The p–i–n junction containing the QDs had a diode like characteristics with reverse bias breakdown voltages $\geq$10 V at 300 K. The 2D electron channel was characterized using magneto transport techniques with an electron densitiy of $N_s = 3.4 \times 10^{11}$ cm$^{-2}$.

The top part of Fig. 19a (“write”) shows a schematic representation of the device band diagram in the growth ($z$) direction, for a situation where the back p-contact is maintained at the same electric potential as the 2DEG channel by the external circuit. By illuminating the sample with monochromatic light, the QD ensemble is selectively excited as described above. As a consequence of the internal electric field in this asymmetric hetero-type p–n junction, tunneling escape is much more likely for holes when compared to electrons. This asymmetry is a natural consequence of the sample design, which provides a GaAs barrier for holes towards the p-type back contact and an $Al_{0.3}Ga_{0.7}As$ barrier with exponentially reduced transmission for electrons towards the 2DEG. Electrons remain

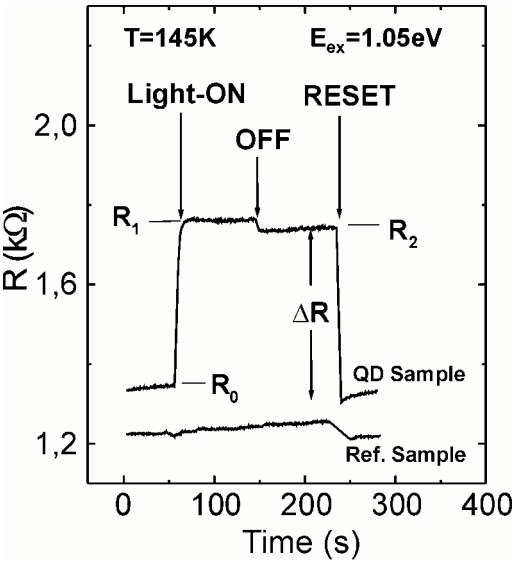


**Fig. 21** Typical write (light on to light off), store (light off to reset), and reset cycle for a structure containing QDs (top) and reference sample (bottom).

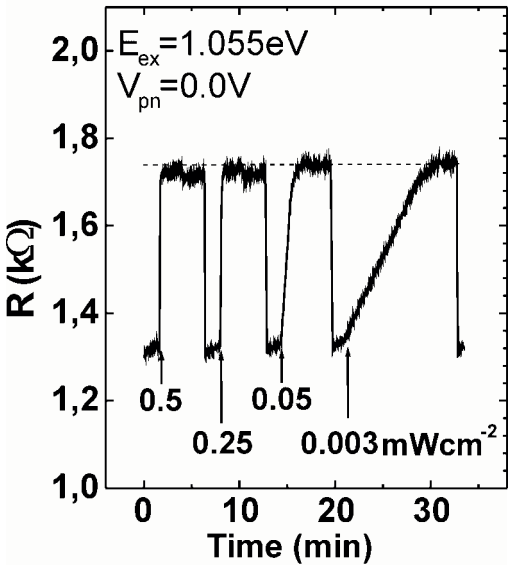


**Fig. 22** Write-store-reset cycles for various excitation power densities.

therefore stored within the QD layer and will change the lateral resistivity of the 2DEG channel. The corresponding situation is depicted in the central part of Fig. 20b (“store”). The photo-generated charge in the QDs can be erased by application of a positive reset pulse $V_{pn} = 1.5$ V on the back contact with respect to the 2DEG (see Fig. 19c “erase”).

A corresponding device structure view is shown in Fig. 20(a) to (c). Near infrared illumination results in electron–hole pair generation within a subset of the InAs QD-ensemble a). After hole tunneling escape, the remaining electrons in the QDs are stored and cause a carrier depletion in the 2DEG channel (b). The stored electron density in the QDs will determine the amount of depletion in the channel and hence the resulting resistance change in a monotonic way, as expected for FET structures. The application of a reset pulse $V_{pn}$ will result in a drift of holes towards the QD layer, where they are captured. This in turn erases the stored electrons by radiative recombination (c). At the end of the reset pulse, surplus holes will again tunnel out of the QDs, leaving the structure back in its initial (pre-illumination) value.

To demonstrate charge storage effects in the device structure, time dependent resistance measurements are presented in Fig. 21. The measurements consist of a 100 s long illumination phase after which the illumination is switched off during a 100 s duration storage period. After this phase, the stored chage is removed via the reset pulse. Illumination at $E_{ex} = 1.05$ eV results in an increase of the channel resistivity $\Delta R = R_1 - R_0$ of $\sim$25% with respect to the initial value $R_0$. At the beginning of the storage period (light off) $\Delta R$ exhibits a weak recovery but remains constant thereafter over the 100 s timescale at $T = 145$ K. The reset pulse switches the device back to its initial state, the channel resistance returning to its pre-illumination value. It is important to note, that a reference sample grown with an identical layer sequence, but without the QD layer shows effectively no such storage effects (see Fig. 21). The charging rate of the QD layer is naturally dependent on the incident optical power density, as shown for $E_{ex} = 1.055$ eV in Fig. 22. Whereas the slope of the temporal resistance change systematically decreases on a reduction of the optical power density from 0.5 mW/cm$^2$ to 0.003 mW/cm$^2$, the final saturation value of the channel resistance is unchanged for the selected bias conditions indicating that the same amount of charge is stored. A more detailed analysis (AFM data of the QD

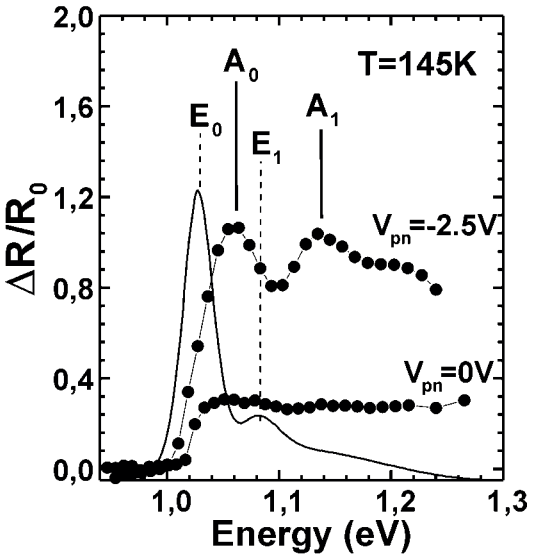


**Fig. 23** Spectral dependence of the photo-effect for different $V_{\mathrm{pn}}$. PL data is shown for comparison (full line).

surface density and modelling of the depletion effects on the 2DEG channel) shows, that the QD density is in the range of $1.5 \times 10^{10}$ cm$^{-2}$, whereas the saturated surface density of the stored charge is in the range of $1.1 \times 10^{10}$ cm$^{-2}$ [70]. This observation indicates that, on average, each QD-stores a single electron. However, on the basis of these results we cannot unambiguously differentiate between whether a smaller fraction of QDs is multiply charged or, indeed, if excitation mechanisms exist that charge QDs at energies away from $E_{\mathrm{ex}}$ and thus, on average, distribute charge over the whole ensemble.

In order to experimentally address this problem, we investigated the dependence of the photoresponse on the energy of laser excitation $E_{\mathrm{ex}}$. The results obtained are presented in Fig. 23 in which the instantaneous photoresponse $\Delta R$ of the ensemble for a range of excitation energies is compared with the interband photoluminescence (PL) which represents the inhomogeneous broadening. The PL response (full line) arises from the recombination of excitons localized in the QDs the two peaks correspond to ground ($E_0$) and first excited state ($E_1$) emission, respectively. The onset of the photoresistance effect observed for $E_{\mathrm{ex}} \sim 1$ eV clearly coincides with the direct excitation into the ground state. In the following, we demonstrate that phonon assisted processes are involved in the QD charging process. As the vertical p–i–n junction is more strongly reverse biased, the 2DEG channel becomes progressively depleted and consequently the magnitude of the observed photoresponse becomes strongly enhanced $\left(\dfrac{\Delta R}{R_0} \geq 100\% \text{ at } V_{\mathrm{pn}} = 2.5 \text{ V}\right)$. Moreover, pronounced peaks labelled $A_0$ and $A_1$ become more clearly resolved from the background. The energy separation between $A_0$ and $A_1$ is $\sim$75 meV, larger than the splitting between the ground and excited state of the PL emission ($E_1 - E_0 \sim 60$ meV). Furthermore, these resonances are shifted from $E_0$ by 33 and 115 meV for $A_0$ and $A_1$, respectively. This indicates that they do not simply reflect the direct excitation of ground and excited QD states. The results shown in Fig. 23 reflect the saturation value of the channel resistance. Thus, all possible excitation mechanisms are included irrespective of the relative absorption probabilities for individual processes. The energy shift between $E_0$ and $A_0$ is 33 meV, which is close to the LO phonon energy expected for InAs QDs in GaAs. The participation of inelastic processes in optical QD excitation has been observed using PL excitation (PLE) spectroscopy on both large ensembles [73] and single dots [74] with a number of vibrational modes involved. Thus, a high density of QD states may accessible via inelastic excitation processes, possibly accounting for the relatively large charge storage densities following resonant optical excitation. A more direct manifestation of this interpretation towards phonon-assisted absorption will follow in the next section when device structures with true optical readout are discussed.

On the basis of the presently discussed InAs/GaAs structures, optically stimulated charge storage effects are found to be persistent over timescales of hours for lattice temperatures below 150 K. At elevated temperatures, thermal loss of stored charge is reduces the storage times. At room temperature, storage times up to $\sim$0.5 ms have been observed [75], which are comparable to charge storage times in modern DRAM memory devices. Significant improvements can be expected in the near future from different III/V semiconductor material systems that offer larger band offsets [77].

### 5.3 QD optical memory structure with optical readout

The memory device discussed in the previous section was designed for optical write and electric readout. In this section we present a fully optical wavelength selective QD-based charge storage device. Resonant data storage at $T = 10$ K is achieved over extremely long timescales $\gg 25$ μs at low temperatures and the principle of wavelength domain data storage using QDs is confirmed unambiguously.

The bandstructure and operating principles of our optical memory device are presented in Fig. 24. A single layer of InGaAs QDs is embedded within the intrinsic region of either an n- or p-type Schottky photodiode for hole or electron storage, respectively. In the write condition (Fig. 24a), the device is unbiased ($V_{\text{write}} \sim 0$ V). Following resonant optical excitation in the region of the QD-groundstates only a small subset of QDs is expected to be charged. For a given laser energy $E_L = \hbar\omega_{\text{in}}$ ideally only QDs with matching ground state energies will absorb and hence become charged. Since excitonic ground state energies depend on the size and composition a particular dot, subsets of different morphologic stucture will be selectively adressed by writing with different laser energies. Such manipulations can be safely performed, either parallel in time or time multiplexed, providing that the device remains biased in the hold condition ($V_{\text{write}} = 0$ V). Following excitation, the remaining holes remain stored due to the exponentially weaker tunneling probability through the $Al_{0.45}Ga_{0.55}As$ barrier. In this configuration, the memory structure is in the hold-condition (Fig. 24a). The operation of an electron storage device is entirely analogous to the scheme described above. In order to readout the previously written information in the wavelength domain, an energy-maintaining readout scheme has to be employed. This is naturally obtained by spectrally resolved optical detection. The present memory device can be easily switched to the read condition by applying a reset

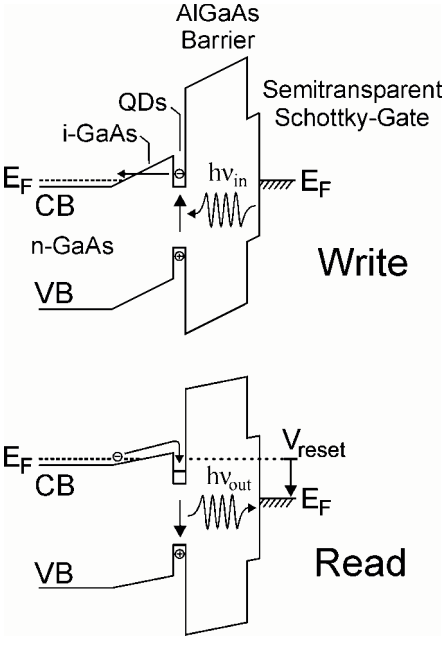


**Fig. 24** Schematic bandstructure and operating principle of the all optical QD-memory structure. Schematic representation of the band structure of the hole storage device with a top-gate bias corresponding to write and read modes.

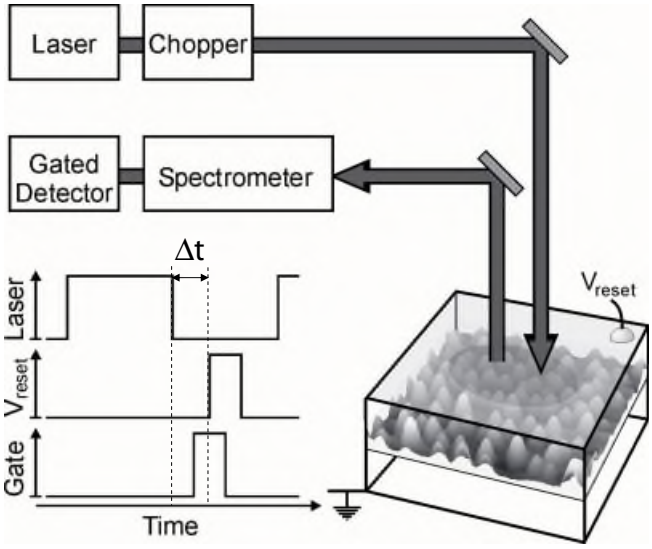


**Fig. 25** Schematic representation of experimental set-up for measurement of all optical QD memory structure.

pulse ($V_{\text{reset}} \geq 0$ V), which brings the Schottky diode into a forward bias condition. At the rising edge of this reset pulse electrons from the n-GaAs back contact drift towards the QD layer and, for charged QDs, result in radiative recombination and photon emission. Light emission occurs therefore only from previously written QDs. Since each QD represents a unique quantum mechanical nano-enviroment and complete relaxation to the groundstate can be safely assumed for the present time scales, the photon energies of the originally employed storage procedure should basically be reproduced. The present device is therefore expected to perform as wavelength domain memory. Further dimensions for information storage are of course available in real space. With typical QD surface densities up to 300 $\mu m^{-2}$, even diffraction limited segmentation or imaging should be possible. The principles of operation described above were realized via experiments performed on MBE grown devices on [100] semi-insulating GaAs substrates. Details of the epitaxial layer sequence and experimental setup can be found in Ref. [76]; here we repeat only details neccessary for the discussion of our experimental results presented below. Experiments were performed using a standard micro-photoluminescence (PL) system and resonant optical excitation pulses were delivered using a mechanically modulated continuous-wave (CW) Ti:sapphire laser ($\hbar\omega_{\text{in}} = 1.25-1.38$ eV) or the Ti:sapphire in combination with a laser diode ($\hbar\omega_{\text{in}} = 1.27$ eV) for two color experiments. All measurements were performed at 10 K using an excitation power density of $P_{\text{exc}} \sim 1$ kW/cm$^2$ unless stated explicitly. An accurately timed sequence of optical (write) and electrical (readout) pulses were applied to the sample at a repetition rate of $\sim$20 kHz as depicted schematically in Fig. 25.

In order to ensure efficient suppression of scattered laser light during detection, a Si-based gated avalanche photodiode was used and only gated on during application of the readout voltage pulse. The charge storage time ($\Delta t$) is defined as the time delay between switching off the optical write pulse and the onset of the electrical readout (Fig. 25). In the present configuration $\Delta t$ could be varied between 1 and 24 μs, defined by the frequency of the mechanical modulation.

Typical charge storage spectra for electron (dashed line) and hole (solid line) devices are presented in Fig. 26 for $\Delta t = 12$ μs. For comparison, the non-resonantly excited PL spectrum ($\Gamma_i \sim 80$ meV FWHM) is also plotted (dotted line). The overall form of the charge storage spectra was found to be very similar for both samples, consisting of two principle components: a sharp peak, labelled R in Fig. 26a, very close to the excitation energy and a much broader band, labeled S, $\sim$20–50 meV to lower energy. For both samples, $\hbar\omega_{\text{in}}$ was tuned to the high-energy side of the QD ensemble ($\sim$1.27 eV) and the magnitude of the readout voltage was +0.8 V corresponding to the onset of majority carrier current flow. The reverse bias storage voltage was carefully optimised between $0 \leq |V_{\text{write}}| \leq 3$V such that the intensity of the charge storage spectra were saturated, corresponding to

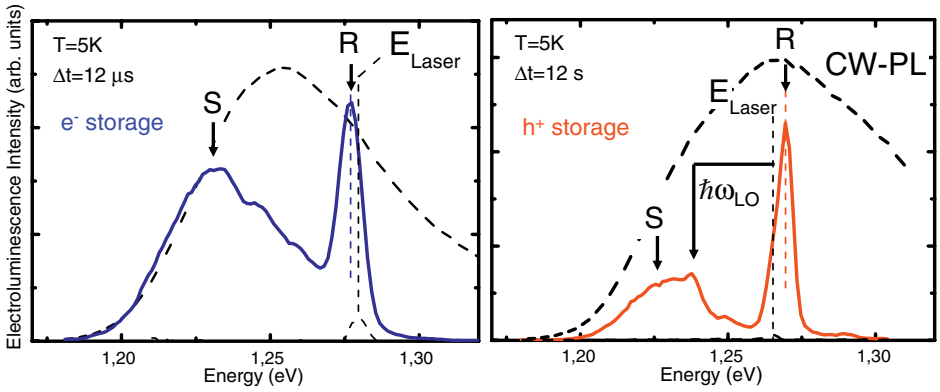


**Fig. 26** Typical emission spectra after application of the reset bias pulse ($\Delta t$ = 12 s), for electrons (dotted line) and holes (continuous line) storage devices, together with the non-resonantly excited QD ensemble luminescence spectrum for comparison (dashed line).

efficient ionization of all photo-generated excitons. Furthermore, no dependence of the luminescence intensity on the duration of the reset pulse was detected indicating that all stored charges contribute to the measured luminescence. The characteristic shape of the charge storage spectra presented in Fig. 26a indicates the existence of two distinct absorption channels. We attribute peak R to direct, selective charging of QD ground states addressable by the excitation laser, a conclusion supported by separate energy-dependent measurements (see below). For such ground states, energy relaxation cannot occur and consequently R arises at an energy ($E_R$) close to $\hbar\omega_{\text{in}}$ (see Fig. 26b). The weak $\sim 5$ meV shift observed between $\hbar\omega_{\text{in}}$ and $E_{\text{R}}$ arises due to the quantum confined Stark effect [49]. The broader, low energy emission band S is attributed to dots that are quasi-resonantly excited via their excited state, a conclusion that is supported by the energy dependent measurements discussed below. During this process, photo-generated excitons relax into their ground state before ionization occurs, resulting in a luminescence band shifted below $\hbar\omega_{\text{in}}$ by the energy separation between ground and excited states. In addition, phonon-assisted excitation may also contribute to S, due to enhanced exciton–LO phonon coupling in QDs as evidenced by the barely resolved satellite features shown in Fig. 26, shifted by $E_{\text{LO}} \sim 32$ meV below $\hbar\omega_{\text{in}}$.

To further investigate the role of these various processes, we recorded charge storage spectra as $\hbar\omega_{\text{in}}$ was tuned from $1.370 - 1.312$ eV, corresponding to shifting the excitation from the peak of the excited state absorption to energies for which only ground state absorption exists. The results are presented in Fig. 27, together with the non-resonantly excited PL and Gaussian fits of the ground and excited state contributions (dashed lines). The most striking effect of shifting $\hbar\omega_{\text{in}}$ to lower energy is the strong reduction of the amplitude of the emission sideband (S) as $\hbar\omega_{\text{in}}$ is shifted below the excited state absorption edge at $\sim$1.32 eV. As a consequence, for all the spectra where $\hbar\omega_{\text{in}} \leq 1.32$ eV in Fig. 27a, peak-R is the dominant emission feature. These observations are consistent with the dominant contribution to S – arising from quasi-resonant charge storage via excited states. However, the quantitative role of phonon-assisted processes cannot be directly clarified by the present observations and a more detailed investigation of these processes will be presented elsewhere.

The carrier dynamics during the charge storage lifetime were investigated by monitoring the temporal development of the form and intensity $I(t)$ of the storage spectrum. As $\Delta t$ increased from 1–24 μs, we observed only a weak decrease of $I(t)$ ($\ll 5\%$) for both electron and hole storage devices. This result clearly demonstrates that the charge storage lifetime is $\gg 25$ μs at $T = 10$ K, in fairly good agreement with our findings for electrical readout presented above. Furthermore, the spectral form of the storage spectra remained completely unchanged as $\Delta t$ increased. No loss of spectral information, such as a transfer of intensity from the resonant peak R to the sideband S was observed, clearly indicating that the stored charge remains in the dots where they were generated without redis-

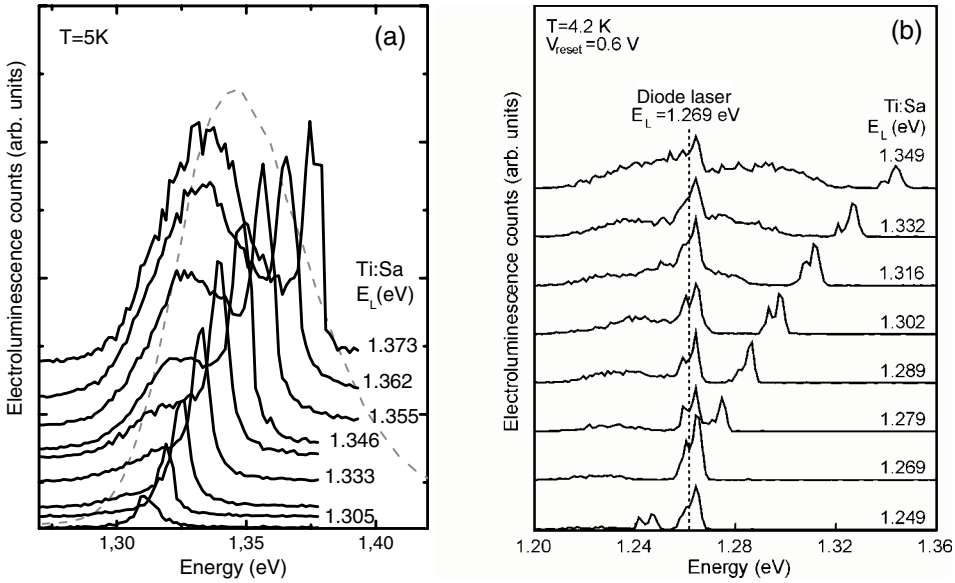


**Fig. 27** a) Storage spectra recorded as a function of $\hbar\omega_{\rm in}$ for different $E_L$ values show the influence of excited state absorption. b) Two color experiment: series of spectra with different excitation energy pairs.

tribution. Finally, in order to demonstrate wavelength selective charge storage we performed two-color experiments, applying a sequence of optical pulses during each excitation cycle. The first pulse, delivered by a diode laser, was centred at $\sim$1.27 eV whilst the second pulse from the Ti:sapphire, at $\hbar\omega_{\rm in}$, was tuned over the ground state absorption spectrum. Charge storage spectra after $\Delta t$ = 12 μs are presented in Fig. 27b. For both excitation energies the emission spectrum has the form described above, consisting of a resonant peak R close to each excitation energy and a weak low energy side band S. In full agreement with the discussion above, the side band intensity increases as $\hbar\omega_{\rm in}$ is shifted into the region of excited state absorption. These results demonstrate unambiguously that two separate and distinct sub-ensembles are charged by the two-excitation frequencies, reaffirming the conceptual basis for implementation of wavelength division multiplexing for information storage using inhomogeneously broadened media such as QDs. It is also remarkable that, for excitation intensities well below saturation as is for the case for the data presented here, crossing of these energies results in a superposition of the charge storage signal and no loss of information. Taken togehter, these results are very encouraging and provide a basis for wavelength domain optical memory devices based on semiconductor QDs.

**Acknowledgements** We would like to acknowledge the contributions of a great number of people involved in SFB 348, TPB1 and A17 as scientific staff and via Dipolma and Doctoral theses. These include: Karl Brunner, Liewen Chu, Frank Findeis, Doris Heinrich, Thomas Asperger, Eric Duijs, Jann Hoffmann and Stefan Stuffler for their contributions to work on semiconductor quantum dots.

## References

[1] S. M. Reimann and M. Manninen, Rev. Mod. Phys. **74**, 1283 (2002).
[2] K. Brunner, U. Bockelmann, G. Abstreiter, M. Walther, G. Böhm, G. Tränkle, and G. Weimann, Phys. Rev. Lett. **69**, 3216 (1992).
[3] K. Brunner, G. Abstreiter, G. Böhm, G. Tränkle, and G. Weimann, Appl. Phys. Lett. **64**, 3320 (1994).
[4] K. Brunner, G. Abstreiter, G. Böhm, G. Tränkle, and G. Weimann, Phys. Rev. Lett. **73**, 1138 (1994).

[5] G. Abstreiter, P. Schittenhelm, C. Engel, E. Silveira, A. Zrenner, D. Meertens, and W. Jäger. Semicond. Sci. Technol. **11**, 1521 (1996).
[6] A. Zrenner, L. V. Butov, M. Hagn, G. Abstreiter, G. Böhm, and G. Weimann, Phys. Rev. Lett. **72**, 3382 (1994).
[7] T. Demel, D. Heitmann, P. Grambow, and K. Ploog, Phys. Rev. Lett. **64**, 788 (1990).
[8] Y. W. Mo, D. E. Savage, B. S. Swartzentruber, and M. G. Lagally, Phys. Rev. Lett. **65**, 1020 (1990).
[9] I. N. Stranski and L. von Krastanow, Akad. Wiss. Lit. Mainz Math. Naturwiss. Kl. IIb **146**, 797 (1939).
[10] D. Leonard, M. Krishnamurthy, C. M. Reaves, S. P. Denbaars, and P. M. Petroff, Appl. Phys. Lett. **63**, 3203 (1993).
[11] Optische und Elektronische Eigenschaften von Selbstorganisierten Quantenpunkten, Doctoral Thesis, Markus Arzberger, TU-München, 2000.
[12] S. Fafard, Z. Wasilewski, J. McCaffrey, S. Raymond, and S. Charbonneau, Appl. Phys. Lett. **68**, 991 (1996).
[13] B. R. Bennett, R. Magno, and B. V. Shanabrook, Appl. Phys. Lett. **68**, 505 (1996).
[14] E. Alphandry, R. J. Nicholas, N. J. Mason, and B. Zhang, Appl. Phys. Lett. **74**, 2041 (1999).
[15] M. C. H. Liao, Y. H. Change, C. C. Tsai, M. H. Chieng, and Y. F. Chen, J. Appl. Phys. **86**, 4694 (1999).
[16] T. I. Kamins, G. Medeiro-Ribeiro, D. A. A. Ohlberg, and R. S. Williams, J. Appl. Phys. **85**, 1159 (1999).
[17] V. A. Shchukin, N. N. Ledentsov, P. S. Kop'ev, and D. Bimberg, Phys. Rev. Lett. **75**, 2968 (1995).
[18] T. S. Kuan and S. S. Iyer, Appl. Phys. Lett. **59**, 2242 (1991).
[19] H. Heidemeyer, S. Kiravittaya, C. Müller, N. Y. Jin-Phillipp, and O. G. Schmidt Appl. Phys. Lett. **80**, 1544 (2002).
[20] For an overview see: A. Zrenner, J. Chem. Phys. **112**, 7790 (2000), and references therein.
[21] D. Gammon, Al. L. Efros, T. A. Kennedy, M. Rosen, D. S. Katzer, D. Park, S. W. Brown, V. L. Korenev, and I. A. Merkulov, Phys. Rev. Lett. **86**, 5176 (2001).
[22] E. Dekel, D. Gershoni, E. Ehrenfreund, D. Spector, J. M. Garcia, and P. M. Petroff, Phys. Rev. Lett. **80**, 4991 (1998).
[23] L. Besombes et al. Phys. Rev. Lett. **80**, 4991 (1998).
[24] D. Loss and D. P. Divicenzo, Phys. Rev. A **57**, 120 (1998).
[25] Q. Xie, A. Madhukar, P. Chen, and N. P. Kobayashi, Phys. Rev. Lett. **75**, 2542 (1995).
[26] J. Tersoff C. Teichert, and M. G. Lagally, Phys. Rev. Lett. **76**, 1675 (1996).
[27] V. Le Thanh, V. Yam, P. Boucaud, F. Fortuna, C. Ulysse, D. Bouchier, L. Vervoort, and J.-M. Lourtioz, Phys. Rev. B **60**, 5851 (1999).
[28] M. Bayer, P. Hawrylak, K. Hinzer, S. Fafard, M. Korkusinski, Z. R. Wasilewski, O. Stern, and A. Forchel, Science **291**, 451 (2001).
[29] P. Borri, W. Langbein, S. Schneider, U. Woggon, R. L. Sellin, D. Ouyang, and D. Bimberg, Phys. Rev. Lett. **87**, 157401 (2001).
[30] P. Borri, W. Langbein, U. Woggon, M. Schwab, M. Bayer, S. Fafard, Z. Wasilewski, and P. Hawrylak, Phys. Rev. Lett. **91**, 267401 (2003).
[31] T. H. Stievater, X. Q. Li, D. G. Steel, D. Gammon, D. S. Katzer, D. Park, C. Piermarocchi, L. J. Sham, Phys. Rev. Lett. **87**, 133603 (2001).
[32] E. Beham, A. Zrenner, S. Stufler, F. Findeis, M. Bichler, and G. Abstreiter, Physica E **16**, 59 (2003).
[33] E. Beham, A. Zrenner, F. Findeis, M. Bichler, and G. Abstreiter, phys. stat. sol. (b) **238**, 366 (2003).
[34] A. Zrenner, E. Beham, S. Stufler, F. Findeis, M. Bichler, and G. Abstreiter, Nature **418**, 612 (2002).
[35] A. Barenco, D. Deutsch, A. Ekert, and R. Josa, Phys. Rev. Lett. **74**, 4083 (1995).
[36] E. Biolatti, R. C. Iotti, P. Zanardi, and F. Rossi, Phys. Rev. Lett. **85**, 5647 (2000).
[37] F. Troiani, U. Hohenester, and E. Molinari, Phys. Rev. B **62**, R2263 (2000).
[38] A. Zrenner, German Patent No. DE 100 06 909 C1, April 4, 2001.
[39] R. J. Warburton, C. Schäflein, D. Haft, F. Bickel, A. Lorke, K. Karrai, J. M. Garcia, W. Schoenfeld, and P. M. Petroff, Nature **405**, 926 (2000).
[40] F. Findeis, M. Baier, E. Beham, A. Zrenner, and G. Abstreiter, Appl. Phys. Lett. **78**, 2958 (2001).
[41] F. Findeis, M. Baier, A. Zrenner, M. Bichler, and G. Abstreiter, Phys. Rev. B **63**, 121309(R) (2001).
[42] F. Findeis, M. Baier, A. Zrenner, M. Bichler, G. Abstreiter, U. Hohenester, and E. Molinari, Phys. Rev. B **63**, 121309(R) (2001).
[43] J. J. Finley, P. W. Fry, A. D. Ashmore, A. Lematre, A. I. Tartakovskii, R. Oulton, D. J. Mowbray, M. S. Skolnick, M. Hopkinson, P. D. Buckle, and P. A. Maksym, Phys. Rev. B **63**, 161305(R) (2001).
[44] M. Markmann, A. Zrenner, G. Böhm, and G. Abstreiter, phys. stat. sol. (a) **164**, 301 (1997).
[45] A. Zrenner, A. Schaller, M. Markmann, M. Hagn, M. Arzberger, D. Henry, G. Abstreiter, G. Böhm, and G. Weimann, Appl. Surf. Sci. **123/124**, 356 (1998).

[46] Z. Yuan, B. E. Kardynal, R. M. Stevenson, A. J. Shields, C. J. Lobo, K. Cooper, N. S. Beattie, D. A. Ritchie, and M. Pepper, Science **295**, 102 (2001).
[47] E. Beham, A. Zrenner, F. Findeis, M. Bichler, and G. Abstreiter, Appl. Phys. Lett. **79**, 2808 (2001).
[48] E. Beham, A. Zrenner, and G. Böhm, Physica E **7**, 359 (2000).
[49] P. W. Fry, I. E. Itskevich, D. J. Mowbray, M. S. Skolnik, J. J. Finley, J. A. Barker, E. P. O'Reilly, L. R. Wilson, I. A. Larkin, P. A. Maksym, M. Hopkinson, M. Al-Khafaji, J. P. R. David, A. G. Cullis, G. Hill, and J. C. Clark, Phys. Rev. Lett. **84**, 733 (2000).
[50] L. Allen and J. H. Eberly, Optical Resonance and Two-Level Atoms (Wiley, New York, 1975).
[51] L. Landin, M. S. Miller, M.-E. Pistol, C. E. Pryor, L. Samuelson, Science **280**, 262 (1998).
[52] A. Yariv, Optical Electronics (CBS College Publishing, 1985).
[53] I. I. Rabi, Phys. Rev. **51**, 652 (1937).
[54] H. Kamada, H. Gotoh, J. Temmyo, T. Takagahara, and H. Ando, Phys. Rev. Lett. **87**, 247401 (2001).
[55] H. Htoon, T. Takagahara, D. Kulik, O. Baklenov, A. L. Holmes, Jr., and C. K. Shih, Phys. Rev. Lett. **88**, 087401 (2002).
[56] M. Betz, S. Trumm, A. Leitenstorfer, E. Beham, H. Krenner, M. Bichler, A. Zrenner, and G. Abstreiter, phys. stat. sol. (b) **233**, 401 (2002).
[57] B. Szafran, S. Bednarek, and J. Adamowski, Phys. Rev. B **64**, 125301 (2001).
[58] J. Brault, M. Gendry, G. Grenet, G. Hollinger, Y. Desires, and T. Benyattou, Appl. Phys. Lett. **73**, 2932 (1998).
[59] E. Duijs, F. Findeis, A. Zrenner, M. Bichler, and G. Abstreiter, phys. stat. sol. (b) **224**, 47 (2001).
[60] C. Fürst, A. Leitenstorfer, and A. Laubereau, IEEE J. Sel. Top. Quantum Electron. **2**, 473 (1996).
[61] R. Grote, and H. Fouckhardt, Opt. Express **4**, 328 (1999).
[62] D. V. Regelman, E. Dekel, D. Gershoni, E. Ehrenfreund, A. J. Williamson, J. Shumway, A. Zunger, W. Schoenfeld, and P. M. Petroff, Phys. Rev. B **64**, 165301 (2001).
[63] D. Bimberg, M. Grundmann, and N. N. Ledentsov, Quantum Dot Heterostructures (Wiley, New York, 1999).
[64] U. Hohenester, F. Rossi, and E. Molinari, Solid State Commun. **111**, 187 (1999).
[65] P. Hawrylak, Phys. Rev. B **60**, 5597 (1999).
[66] S. Muto, Jpn. J. Appl. Phys., Part 2 **34**, L210 (1995).
[67] J. E. Golub, K. Kash, J. P. Harbison, and L. T. Florez, Phys. Rev. B **41**, 8564 (1990).
[68] S. Zimmermann, A. Wixforth, J. P. Kotthaus, W. Wegscheider, and M. Bichler, Science **283**, 1292 (1998).
[69] G. Yusa and H. Sakaki, Appl. Phys. Lett. **70**, 345 (1997).
[70] J. J. Finley, M. Skalitz, M. Arzberger, A. Zrenner, G. Böhm, and G. Abstreiter, Appl. Phys. Lett. **73**, 2618 (1998).
[71] A. J. Shields, M. P. O'Sullivan, I. Farrer, D. A. Ritchie, R. A. Hogg, M. L. Leadbeater, C. E. Norman, and M. Pepper, Appl. Phys. Lett. **76**, 3673 (2000).
[72] T. Lundstrom, W. Schoenfeld, H. Lee, and P. M. Petroff, Science **286**, 2312 (1999).
[73] M. J. Steer, D. J. Mowbray, W. R. Tribe, M. S. Skolnick, and M. D. Sturge, Phys. Rev. B **54**, 17738 (1996).
[74] F. Findeis, A. Zrenner, G. Böhm, and G. Abstreiter, Phys. Rev. B **61**, R10579 (2000).
[75] K. Imamura, Y. Sugiyama, Y. Nakata, S. Muto, and N. Yokoyama, Jpn. J. Appl. Phys. **34**, L1445 (1995).
[76] M. Kroutvar, Y. Ducommun, J. J. Finley, M. Bichler, A. Zrenner, and G. Abstreiter, Appl. Phys. Lett. **83**, 443 (2003).
[77] H. Pettersson, L. Bt, N. Carlsson, W. Seifert, and L. Samuelson, Appl. Phys. Lett. **79**, 78 (2001).